UNIVERSITÀ DEGLI STUDI DI PADOVA

Dipartimento di Fisica e Astronomia "Galileo Galilei"

Master Degree in Physics

Final Dissertation

Study of beam-gas interaction at the LHC for the Physics Beyond Collider Fixed-Target study

Thesis supervisor

Prof. Marco Zanetti

Thesis co-supervisor

Dr. Roderik Bruce

Candidate

Caterina Boscolo Meneguolo

Academic Year 2019/2020

Contents

CHAPTER 1

The LHC and the Physics Beyond Collider Fixed-Target study

The *Conseil Européen pour la Recherche Nucléaire* (CERN) was founded in 1954 from a collaboration of 12 countries, with the aim of providing researchers with state-of-the-art accelerator facilities to investigate the frontiers of fundamental physics. It presently includes 23 Member States and many other partner states co-operating at different levels [1].

The CERN complex (Fig. 1.1) hosts the Large Hadron Collider (LHC), presently world largest particle accelerator with its 27-km-long circumference. It is built at a mean depth of 100 m under the French-Swiss border between the Jura mountains and Lake Geneva. It is active since 2008.

In the LHC two particle beams are accelerated in opposite directions and made to collide producing the conditions to create new particles, allowing to study in detail their characteristics and interactions thanks to particle detectors. During the years of LHC activity, many observations have increased our knowledge of the Standard Model and the history of the universe, including the discovery of the Higgs boson in 2012 [2, 3].

1.1 The LHC performance

After going through the sequence of linear and circular accelerators composing the injection chain, two proton beams are injected in the LHC, running in opposite directions in separated beam lines where an ultra-high vacuum (10^{-13} atm) is maintained.

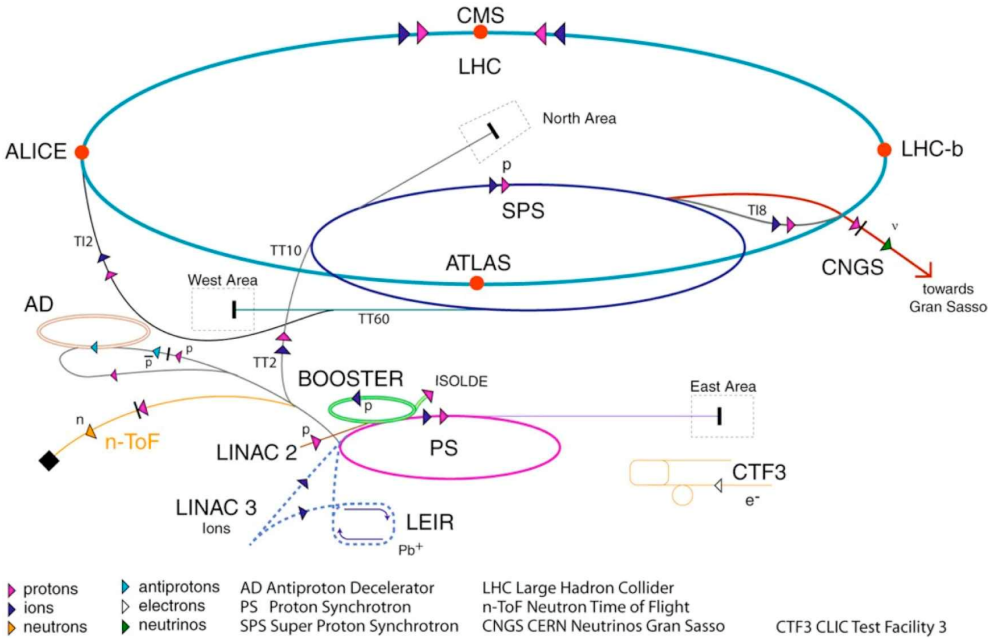

FIGURE 1.1: Layout of the full CERN accelerator complex, with the LHC injection chain. The proton accelerator chain starts with LINAC2, where protons are taken from hydrogen and accelerated in a RF quadrupole followed by a tube linear accelerator, until they get a kinetic energy of 50 MeV. The protons are then injected into the Proton Synchrotron Booster—composed of four superimposed rings—where they reach an energy of 1.4 GeV. In the Proton Synchrotron (PS) ring they are accelerated to a momentum of 26 GeV/c, and subsequently they pass through the Super Proton Synchrotron (SPS) where they get accelerated to 450 GeV/c and are finally ready to be extracted and injected in the LHC. Heavy ions instead are preaccelerated in the LINAC 3, in the Low Energy Ion Ring (LEIR) they are accelerated up to 72 MeV/u and collected in bunches and then they passe to the PS and SPS for further acceleration, bunch adjustment and electron stripping, before being injected in the LHC at an energy of 177 GeV/u. Credits: CERN.

A scheme of the injection chain is given in Fig. 1.1. The beam rotating clockwise is called Beam 1 (B1) and the one rotating counterclockwise is called Beam 2 (B2)

The beams are further accelerated in the LHC ring thanks to radio-frequency (RF) cavities, so they can reach and maintain the top energy. Design energy is 7 TeV per beam—i.e., head-on collisions taking place at 14 TeV centre of mass energy—and the operational top energy was progressively increased since the LHC start from 3.5-4 TeV during Run-1 (2009-2013), to 6.5 TeV per beam in Run-2 (2015-2018).

Besides protons, a series of runs has been dedicated to the heavy-ion collision program since the start of LHC activity. Lead nuclei (but also other ions are possible) follow a dedicate injection chain before being injected in the LHC, in order to perform Pb–Pb or p–Pb collisions. This kind of interaction is particularly interesting for reproducing and studying the quark-gluon plasma that was present at the early stages of the universe. In the last heavy-ion run of 2018 a beam energy of 2.51 TeV/u was achieved, with the aim of reaching 2.76 TeV/u in the future.

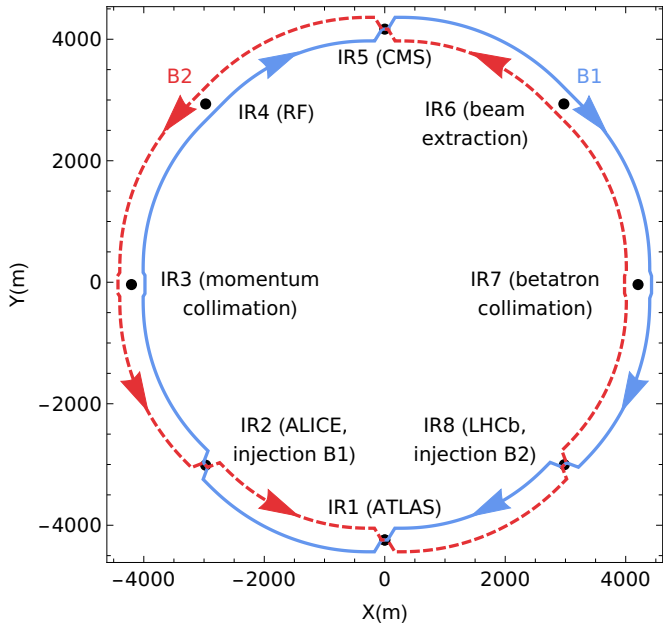

FIGURE 1.2: LHC Interaction Regions (IRs). From [4].

Superconducting magnets are responsible of bending and stabilising the beam trajectory, while magnetic lenses keep the beam focused in the transverse plane. Collimators are installed along the circumference to remove particles that deviate from the desired trajectory, preventing their impact on sensitive equipment.

The LHC contains eight arcs and eight straight sections, the so-called insertion regions (IRs), hosting the injection and extraction systems, the major collimation sectors, RF cavities and the four points where the beams are made to collide—named the Interaction Points (IPs)—corresponding to detector sites of the four main experiments: ATLAS, ALICE, CMS and LHCb. A basic scheme of the LHC circumference with its IRs is shown in Fig. 1.2.

Accelerators are built to investigate events with an occurrence probability that usually varies with energy, and is often very low. A characterizing parameter for a particle collider is its ability to collect interesting events in a given amount of time. This is because they have to be collected in large quantities before claiming a discovery—conversely, a great number of collisions without the occurrence of the studied event have to be recorded in order to safely exclude the energy range for that event.

The key quantity expressing this ability is the integrated luminosity. It strongly depends on the instantaneous luminosity ($\mathcal{L}$), which is defined as the counting rate of events for a process of unit cross section. The instantaneous luminosity is independent from the events of interest, but it depends on machine parameters, like the number of particles in the beam, the frequency of beam revolution around the ring, and the beam transverse area. The factors that determine luminosity in a collider will be discussed in details in Section 1.3.2. At the time of writing (i.e., after the end of LHC Run II), the actual peak luminosity achieved is $\mathcal{L} \sim 2.1 \times 10^{34}\ \mathrm{cm}^{-2}\mathrm{s}^{-1}$.

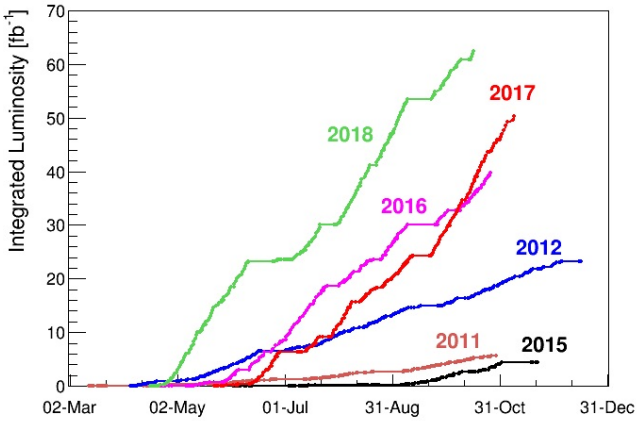

FIGURE 1.3: The integrated luminosity delivered to the ATLAS and CMS experiments during different LHC runs. The 2018 run produced 65 inverse femtobarns of data, which is 16 points more than in 2017. Credits: CERN.

As the accelerator parameters vary through time and the data acquisition is subdued to the machine program schedule, the most significant quantity expressing the performance of the accelerator is the luminosity integrated over the lifetime of the experiment. It depends also on the limits on peak luminosity and on the machine availability (i.e., how often any faults occur and how long they are). In Fig. 1.3 it is presented the year-by-year evolution of integrated luminosity as delivered to ATLAS and CMS experiments (the highest luminosity is demanded and achieved in collision points IP1 and IP5)[1].

1.1.1 The High-Luminosity Upgrade

To extend the LHC discovery potential, a major upgrade will be performed to increase the accelerator luminosity by a factor 5 beyond its design value—the HL-LHC goal is 5×10^{34} cm^{-2}s^{-1}—after 2025 [5].

The luminosity improvement will be achieved thanks to challenging innovative technologies; among them, the 11–12 T superconducting magnets made of a niobium-tin alloy (present Nb-Ti magnets "only" provide 8 T), like the large-aperture Nb_3Sn quadrupoles in the triplets. In addition, very compact superconducting RF cavities for beam rotation with ultra-precise phase control, called crab-cavities, will allow major overlap of the colliding bunches at the IPs. While new technology for beam collimation, and long high-power superconducting links with zero energy dissipation will allow to stand the new machine performance without damages [6].

The Hign Luminosity LHC (HL-LHC) project began in 2011 involving many laboratories from CERN member states and some external countries. The project was announced as the top priority of the European Strategy for Particle Physics in 2013. In April 2018, civil-engineering work started.

[1] Let us recall the handy conversion: 1 b = 10^{-24} cm^2.

1.2 The Physics Beyond Collider Study Program

While colliding particles at higher and higher energies is considered one of the best ways to search for new phenomena, there are other ways to investigate fundamental physics, involving lower energies and different experimental techniques.

That is the reason why in September 2016 the CERN management launched a study program that has been involving a wide range of physicists from theoretical, experimental and accelerator fields. The mandate of the Physics Beyond Collider (PBC) study [7] specifies that the exploratory study is "aimed at exploiting the full scientific potential of CERN's accelerator complex and its scientific infrastructure through projects complementary to the LHC, HL-LHC and other possible future colliders. These projects would target fundamental physics questions that are similar in spirit to those addressed by high-energy colliders, but that require different types of beams and experiments". Examples of physics goals include searches for rare processes and very-weakly interacting particles, measurements of electric dipole moments, etc.

During the kick-off meeting held in September 2016 a number of areas of interest were identified and working groups were set-up, divided in physics-oriented and accelerator-oriented groups, to pursue studies in these areas. Group meetings take place regularly, with constant monitoring of the scientific activity, and the proposals under study were collected in the *Summary Report of Physics Beyond Colliders at CERN* by the end of 2018 (see ref. [8]).

Under the Physics domain, two sub-groups are responsible of evaluating the physics cases in the fields of Physics Beyond Standard Model (BSM) and Quantum Chromodynamics (QCD).

The expected lifetime of this program reaches 2040, i.e., the entire lifetime of LHC and its High-Luminosity upgrade.

1.2.1 Fixed-Target Experiment Proposals

Among the several groups formed within the PBC study, a working group started to work on some specific proposals to perform fixed-target experiments at the LHC [9]. The proposals foresee scattering experiments on both solid and gaseous targets, polarised or unpolarised, potentially using bent-crystals to channel part of the beam halo[2] towards an internal target located upstream of a forward detector. A scheme of three of the possible experimental setups is reported in Fig. 1.4.

The physical interest in performing solid target collisions, with crystal halo splitting setup, is to measure the electric and magnetic dipole moments of charged baryons [11, 12]. Instead, gas target experiments are oriented towards the study of the nuclear partonic structure and the quark gluon plasma, together with the production of datasets for hadronic cross sections useful for cosmic ray physics models [13].

A report on the work of the fixed-target working group was recently published: [14]. The installation of a polarised gas target is not foreseen before Long Shutdown 3 (LS3). Instead, the installation of a crystal beam-splitting setup could be considered in LS3.

[2] Particles can be trapped in the potential between crystal planes and follow this potential, even if the plane is slightly bent. For further details see Ref. [10]

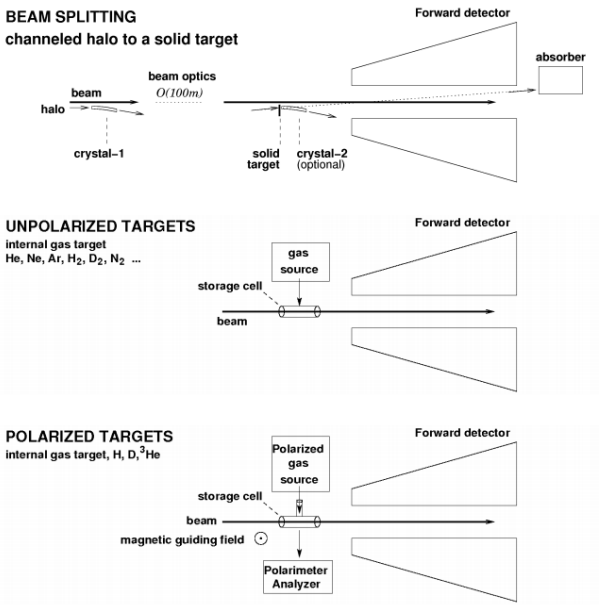

FIGURE 1.4: Sketches of three fixed target setups: crystal beam splitting for a double-crystal setup (top) and unpolarized (middle) and polarized (bottom) gaseous targets. From [9].

Thus, we must assume for the studies that the full HL-LHC upgrades have been implemented by the time the PBC proposals could be put into effect.

1.2.1.1 Gas target at LHCb

The subject of this thesis is a feasibility study—from the point of view of the machine safety—of a proposed gas target experiment at the LHCb detector at IP8 (see Fig. 1.5 for a schematic view of the detector) after the HL-LHC upgrade. The LHCb forward orientation perfectly suits the job of revealing the products of beam collision on a fixed-target installed upstream the detector itself. Nevertheless, a rich fixed-target physics program has already been performed at IP8 exploiting a gas injection system, SMOG, originally conceived to perform luminosity scan of the colliding beams. Examples of interesting results are found at [15, 16, 17].

Referring to Fig. 1.5, the internal gas target would be installed close to the left edge of the VErtex Locator (VELO) subdetector. The VELO consists of a series of silicon modules arranged along the beam direction, which provide precise measurements of track coordinates close to the interaction region, for the identification of displaced secondary vertices [18]. The detectors are mounted in a vessel that maintains vacuum around the sensors and is separated from the machine vacuum by a thin walled corrugated aluminum sheet called the RF foil. It is installed around the collision point, with the IP slightly off-centered away from the LHCb detector core.

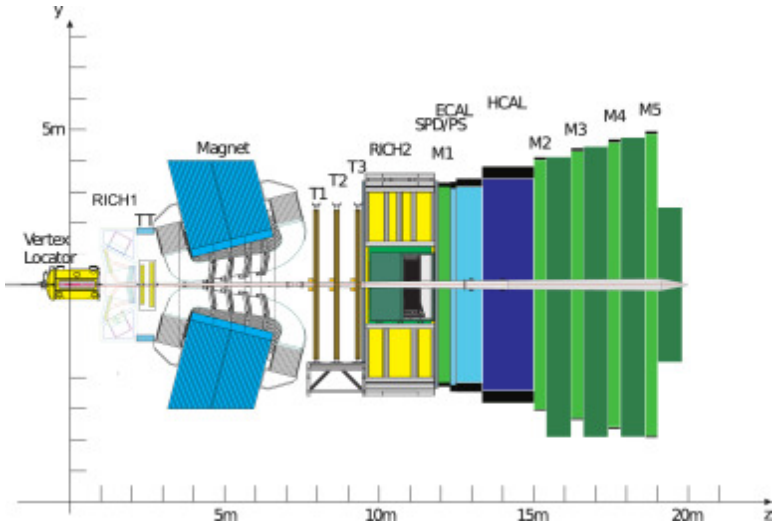

FIGURE 1.5: Schematic view of the LHCb detector. Side view. Credits: LHCb Collaboration.

1.2.1.2 Storage Cell

The performance of gas target experiments is improved implementing a storage cell (SC), i.e., a cylindrical open-ended tube traversed by the beam inside which the target gas is injected. Details on the SC technology can be found at [19]. The gas is injected at the center of the SC via a feed tube and is left to flow towards the two ends of the cell assuming a triangular-shaped density profile as schematized in Fig. 1.6. After flowing out from the edges, turbo-molecular pumps maintain a 10^{-7} mbar vacuum in the beam pipe.

The improvement brought by the introduction of a storage cell is the possibility of enhancing the target density up to about $\theta = 10^{14}$ atoms/cm^2—two order of magnitude larger than SMOG—preserving the high-quality vacuum outside. Nevertheless, in the SC a variety of gas species can be injected: polarised H, D and ^{3}He and unpolarised H_2, D_2, He, Ne, Ar, Kr, Xe, N_2 and O_2. The storage cell technology has been largely exploited in storage rings within the last decades, for example at DESY and COSY [20, 21]. A storage cell is going to be installed at LHCb during present shutdown (LS2), as part of SMOG technical upgrade (SMOG2 project). Part of the results of the study here reported was used in the writing of SMOG2 technical proposal [22].

1.3 Elements of Beam Dynamics

Circular accelerators, like the LHC and its injection chain, are designed to drive and accelerate charged particles along a desired orbit exploiting the simple and well-known fact that every charged particle facing electrical (E) and magnetic (B) fields is subject to the Lorentz Force:

$$\vec{F} = q(\vec{E} + \vec{v} \times \vec{B}). \tag{1.1}$$

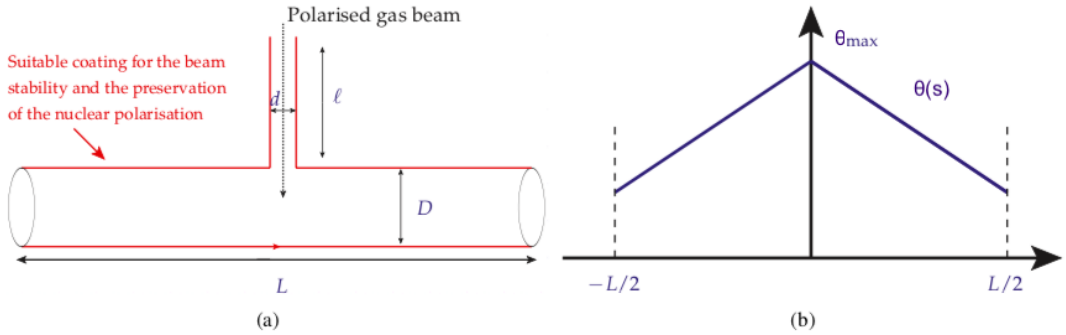

FIGURE 1.6: (a) Schematic view of the target cell. Polarised gas can be injected ballistically - unpolarised gas via a capillary - into the cell center; (b) Gas density profile, ρ(s) along the beam s axis. Credits: C. Hadjidakis.

A particle entering the vacuum pipe of a storage ring is carried through a lattice consisting of accelerating electric fields (in the radio-frequency cavities) together with bending and focussing magnetic forces. The combination of bending and focussing magnets defines a magnetic guide field, in which particles at nominal energy E_0 would follow forever an ideal closed orbit, approximately circular.

The RF cavities provide the particles with energy needed to reach the top energy and to compensate any loss (due, for example, to synchrotron radiation). Every proton traversing a cavity sees a 2 MV voltage oscillating with 400 MHz frequency, per eight subsequent cavities.The whole ramp from 450 GeV to 6.5 TeV takes about 20 minutes, with the beam passing through the RF cavities around one million times. Once at top energy, the protons with zero synchronous phase will see no more acceleration, while the protons with slightly different energy, arriving earlier or later will be out of phase with respect to the oscillating voltage. This tends to either disperse or collect the protons in tightly bunched bunches, depending on their phase shift.

The resulting beam is thus split in a number of evenly-spaced bunches, in which the protons perform oscillations in both the longitudinal position and the energy. The focussing property of the guide field allows to maintain the off-energy particles of the beam along quasi-periodic, stable trajectories close to the ideal design orbit, making them perform radial and vertical oscillations (betatron oscillations), which are the main subject of this introductory insight. An illustrative description of the physics of charged particle storage rings can be found at [23] and [24].

1.3.1 The Betatron Oscillations

In order to proceed in a brief study of the beam dynamics along the accelerator circumference, we define a handy coordinate system. In the following, the coordinates (s, x, y) will be conventionally used: s, or the azimuthal coordinate, is the cyclic distance along the ideal orbit (given the length L of the orbit, the same point can be equally referred to by s or s+nL, n integer); x and y represent respectively the horizontal (radial) and vertical distance from the ideal orbit, x positive is taken outward, y positive is taken upward. The following study of the behavior of a single particle in the magnetic

guide field discards radiation losses and accelerating fields, as well as all collective effects and two-beam effects faced by charged particles in real beams.

Let us suppose to have a static guide field, the orbit lying on the horizontal plane, and the dipole purely vertical magnetic field $\overrightarrow{B}$, with strength $B_0(s)$ and variation $\left(\frac{\partial B}{\partial x}\right)_{0s}$ along the nominal orbit at s position.

Recalling Maxwell's equations, $\frac{\partial B_x}{\partial y} = \frac{\partial B_y}{\partial x}$, the field felt by a proton at a given position (s,x,y) is given by (in linear approximation):

$$\begin{aligned} B_y(s,x,y) &= B_0(s) + \left(\frac{\partial B}{\partial x}\right)_{0s} x \\ B_x(s,x,y) &= \left(\frac{\partial B}{\partial x}\right)_{0s} y \end{aligned} \tag{1.2}$$

It is convenient to re-scale the fields with respect to the particle nominal energy E_0, since the fields of a storage ring are set in order to obtain progressively the desired operation energy, and the two quantities vary proportionally maintaining the same orbit, which is independent of the operating energy itself. The normalised gradient is defined as:

$$K_0(s) = \frac{ec}{E_0}\left(\frac{\partial B_0}{\partial x}\right)_{0s}. \tag{1.3}$$

with e the electronic charge and c the speed of light. It represents the rate of change of the inverse curvature radius with transverse (radial) displacement.

From a well-defined magnetic guide field it is possible to derive the equation of motion for a proton moving on a trajectory near the design orbit as a function of s, in terms of small x, y. Detailed calculations can be found at [24].

In linear approximation, for a particle with the design momentum the equations of motions are:

$$x'' + \left(K_0 + \frac{1}{\rho_0^2}\right)x = 0 \tag{1.4}$$

$$y'' - K_0 y = 0 \tag{1.5}$$

with ρ_0 the local bending radius (it is nonzero only in the x plane, according to the assumptions we made). Stability in each plane is achieved if the solutions are oscillatory.

It is called weak focussing the condition in which stability is achieved in both horizontal and vertical plane, imposing $0 < -K_0 < \frac{1}{\rho_0^2}$. The oscillatory solution, called betatron oscillations, has a wavelength larger than the accelerator circumference. This represents a limit on the size of possible accelerators, since at larger ρ would correspond larger oscillation amplitudes, requiring larger and larger magnet aperture.

This limit was overcome introducing the so-called strong focussing principle. It consists in alternating sectors with strong horizontal focussing ($K_0 >> \rho_0^2$) and sectors with strong horizontal defocussing ($K_0 << \rho_0^2$). This method allows to increase arbitrarily the number of betatron oscillations around a circumference C, which is defined as

the tune Q= $\frac{C}{\lambda}$ (being λ the wavelength of the betatron oscillation). As a consequence, the betatron amplitude is kept small for increasing radii.

In the LHC, bending and focussing forces are provided by dipole and quadrupole magnets, respectively. A quadrupole magnet provides focussing on one plane and defocussing on the other one. The combination of two quadrupoles with polarity rotated by 90° becomes a system focussing in both planes.

Usually, the period of the periodic functions $K_0(s)$ and $\rho_0(s)$ corresponds to the length of a unitary "cell", repeated N times around the circumference.

Since the motion takes analogous form in x and y, let us treat the general equation of motion

$$u'' = K(s)u \tag{1.6}$$

representing both eq. 1.4 and1.5, with adequate redefinition of the magnetic functions. In each segment in which K(s) assumes a constant value, the motion in u will take the following forms (a, b are constant in each segment):

$$u(s) = \begin{cases} a\cos(\sqrt{K}s + b) & \text{for } K > 0 \\ as + b & \text{for } K = 0 \\ a\cosh(\sqrt{-K}s + b) & \text{for } K < 0 \end{cases} \tag{1.7}$$

There are infinite possible trajectories depending on the initial conditions at a reference point s_0. Any solution of a second order equation such as eq. 1.6 can be written as a linear combination of two independent solutions. Two possible independent solutions are represented by the quasi-periodic "cosine-like" and the "sine-like" trajectories: C(s, s_0) and S(s, s_0). They obey the initial conditions $C(s_0, s_0) = 1$, $C'(s_0, s_0) = 0$, $S(s_0, s_0) = 0$ and $S'(s_0, s_0) = 1$. All possible trajectories can then be written as:

$$u(s) = C(s,\ s_0)u_0 + S(s,\ s_0)u'_0 \tag{1.8}$$

$$u'(s) = C'(s,\ s_0)u_0 + S'(s,\ s_0)u'_0 \tag{1.9}$$

In matrix notation, considering

$$u(s) = \begin{bmatrix} u(s) \\ u'(s) \end{bmatrix}, \tag{1.10}$$

we can write

$$u(s) = M(s, s_0)u(s_0) \tag{1.11}$$

with M(s, s_0) the transfer matrix to s from s_0, defined as:

$$M(s, s_0) = \begin{bmatrix} C(s, s_0) & S(s, s_0) \\ C'(s, s_0) & S'(s, s_0) \end{bmatrix}. \tag{1.12}$$

The transfer matrix for any span of s can be found multiplying the transfer matrices of the segments composing that span. Thus, the problem of determining the trajectory of a particle through a beam line is reduced to the multiplication of transformation matrices through the elements of the beam line.

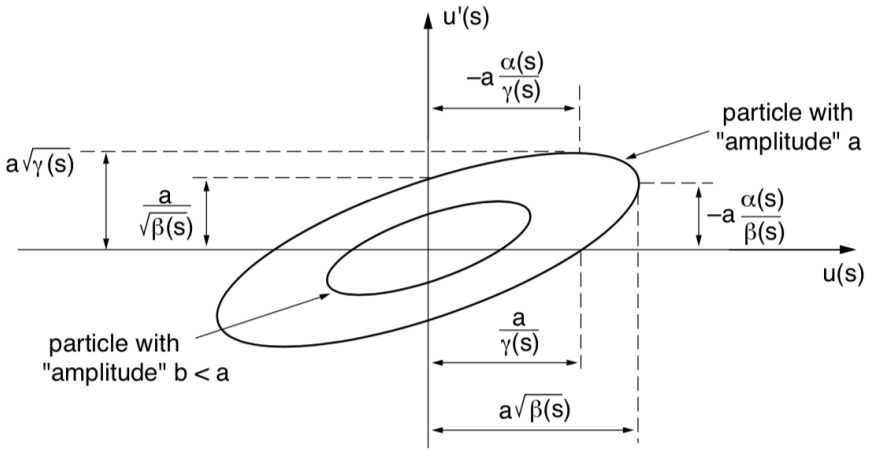

FIGURE 1.7: Phase plane ellipses for particles with different amplitudes. From [24].

More interesting features of beam trajectories can be derived from a pseudo-harmonic approach to the problem. The general solution to equation 1.6 is an oscillating solution with an s-dependent amplitude, and a non-linear s-dependence of the phase:

$$u(s) = \sqrt{a}\sqrt{\beta(s)}\cos[\psi(s) - \psi_0] \tag{1.13}$$

with a and ψ_0 integration constants and $\psi(s)$ defined as

$$\psi(s) = \int_{s_0}^{s} \frac{d\bar{s}}{\beta(\bar{s})}. \tag{1.14}$$

The functions $\beta_x(s)$ and $\beta_y(s)$, known as the betatron functions, are uniquely determined by K(s) and they completely describe the lateral focussing properties of the guide field.

Computing the derivative of 1.13 and defining $\alpha = -\frac{1}{2}\beta'$ and $\gamma = (1+\alpha^2)/\beta$, the so-called Courant-Snyder invariant is obtained:

$$\gamma u^2 + 2\alpha u u' + \beta u'^2 = a^2. \tag{1.15}$$

This can be recognized as the equation of an ellipse in the u–u' plane of area πa^2, where a represents a possible set of omotetic amplitude parameters. The physical meaning of the functions β, α and γ, called the Twiss functions, becomes clear: they correspond to the parameters of an ellipse described by the traveling in phase space of a single particle (see figure 1.7). The form of such an ellipse is changing along the ring circumference, since the parameters are functions of s, but the area remains constant.

It is usually defined the beam emittance ϵ such that, approximating the beam distribution to a double-Gaussian, one standard deviation of the beam particles are enclosed in an ellipse of area $\pi\epsilon$. The betatron oscillation for a particle on the phase ellipse is:

$$u(s) = \sqrt{\epsilon}\sqrt{\beta(s)}\cos[\psi(s) - \psi_0] \tag{1.16}$$

Which gives the equation of the envelope surrounding the specified beam fraction (i.e., one std):

$$E(\mathrm{s}) = \sqrt{\epsilon\beta(\mathrm{s})} \tag{1.17}$$

The betatron oscillation of a single particle along the ring is quasi-periodic, with varying amplitude and frequency. On every machine revolution the particle phase coordinates will remain on the same ellipse. It will occupy cyclically a finite number of points if the tune Q is a rational number, otherwise it will span all the ellipse contour.

The emittance ϵ is a function of particle momentum. In fact, when a beam accelerates, the particle transverse angles shrink, resulting in a diminished beam size in the transverse phase space. As a consequence, it is sometimes useful to talk about *normalised* emittance, $\epsilon_n = \gamma_\mathrm{r}\beta_\mathrm{r}\epsilon$, where the relativistic factors have come to play. The normalised emittance is a constant parameter that efficiently characterizes an accelerator.

Normalized coordinates are frequently used to describe particle motion and will come to play later in this work. They are obtained from the following transformation:

$$\mathrm{u}_n = \frac{\mathrm{u}}{\sqrt{\epsilon\beta(\mathrm{s})}} \qquad\qquad \mathrm{u'}_n = \frac{\alpha(\mathrm{s})}{\sqrt{\epsilon\beta(\mathrm{s})}}\mathrm{u} + \sqrt{\frac{\beta(\mathrm{s})}{\epsilon}}\mathrm{u'} \tag{1.18}$$

The beam envelope describes a unitary radius circumference in the so-normalised phase spaces u_n–$\mathrm{u'}_n$.

1.3.2 Beam size and Luminosity

The emittance defined in previous section allows to define the beam betatron size σ_u, corresponding to one standard deviation:

$$\sigma_\mathrm{u}(\mathrm{s}) = \sqrt{\epsilon\beta_u(\mathrm{s})}, \tag{1.19}$$

and its divergence σ'_u:

$$\sigma'_u(\mathrm{s}) = \sqrt{\epsilon\gamma_u(\mathrm{s})}. \tag{1.20}$$

Particles within $3\sigma_u$ constitute the beam core, while particles outside are called the halo. It is now clear the usefulness of normalising the transverse coordinates to the u_n–$\mathrm{u'}_n$ phase space with 1.18: this action corresponds to expressing the transverse coordinates in units of the beam divergence σ_u.

In addition to the betatron oscillation, the particles in the beam are subject to energy oscillations. In general, the energy of a particle in a storage ring will deviate from the nominal energy and will perform synchrotron oscillation around it. The radial motion can be separated into two parts: $\mathrm{x}(\mathrm{s}) = \mathrm{x}_\beta + \mathrm{x}_\delta$. One part, x_β, is the displacement due to betatron oscillations (on-momentum motion) as derived in Eq. 1.13, while x_δ is a displaced closed curve representing the equilibrium orbit for an off-momentum particle. It is defined as:

$$\mathrm{x}_\delta = \mathrm{D}_x(\mathrm{s})\frac{\Delta p}{p_0}, \tag{1.21}$$

where the dispersion function $D_x(s)$ was introduced.

This effect contributes in enhancing the beam size, the new expression being:

$$\sigma_u^{\text{beam}}(s) = \sqrt{\epsilon\beta_u(s) + \left(D_x(s)\sigma_p\right)^2}, \tag{1.22}$$

σ_p the rms momentum spread of the beam particles. The beam profile is quite well represented by a Gaussian distribution.

In Section 1.1, it was explained how the performance of a particle collider can be expressed in terms of its luminosity $\mathcal{L}$. The treatment performed so-far allows us to understand how LHC luminosity is calculated, considering the realistic beam dimension. Indeed, the luminosity for two beams colliding head-on is given by:

$$\mathcal{L} = \frac{N_1 N_2 n_b f}{A_{\text{eff}}}, \tag{1.23}$$

where $N_{1(2)}$ is the number of particles per bunch, n_b the number of bunches per beam, f the revolution frequency and A_{eff} is the effective area of bunch crossing. For two Gaussian beams this reduces to:

$$\mathcal{L} = \frac{N_b^2 n_b f}{4\pi\sigma_x\sigma_y} \tag{1.24}$$

This is of course an approximation. Real-life beams face several effects, either planned or systematic: crossing angle, collision offset, hour-glass effects, non-Gaussian beam profiles, non-zero dispersion at collision point. A detailed treatment of all these effects can be found at [25]. What can be said in general is that bunches with a smaller transverse size correspond with a larger luminosity. This simple evidence is the reason why the design optics of particle colliders foresee the installation of low-beta inserts, where β is dramatically reduced at the collision points. Due to its relevant impact on experiment performances, the value of the betatron function at the IPs is referred to as β^*.

To give some numbers, some optic parameters for LHC and HL-LHC version 1.3 are listed in Table 1.1 [26]. One can directly calculate with Eq. 1.24 a rough estimate of the peak luminosity for head-on collision at the points with minimum β^* —that is, at IP1 and IP5: $\mathcal{L}_{\text{LHC}} = \frac{N_b^2 n_b c\gamma_r\beta_r}{4L\pi\epsilon_n\beta^*} \sim 10^{34}$ cm^{-2}s^{-1} and $\mathcal{L}_{\text{HL-LHC}} \sim 10^{35}$ cm^{-2}s^{-1}, which guess the correct order of magnitude. Discrepancies are due to the aforementioned effects. A more detailed table of parameters is given in Appendix A.

1.4 Collimation

We are treating the problem of collimation from the point of view of the LHC as it has been operated up to now. The same concepts, with the appropriate modifications due

[3] 2748 bunches colliding in IP1/5

[4] This value refers to the levelled luminosity that would be provided in order to have constant luminosity over many hours.

Parameters	**LHC**	**HL-LHC v1.3**
Beam energy in collision [TeV]	7	7
Relativistic γ	7461	7461
Circumference length [m]	26658.8832	26658.8832
N_b	1.15E+11	2.2E+11
n_b	2808	2760 [3]
β^* at IP1/5 [m]	0.55	0.15
ϵ_n [μm rad]	3.75	2.50
Peak luminosity in IP1/5 [$cm^{-2}s^{-1}$]	1.0E+34	5E+34 [4]

TABLE 1.1: Some design parameters for LHC and HL-LHC in standard 25 ns bunch spacing configuration, version 1.3.

to the foreseen increase in luminosity, apply for the HL-LHC upgrade, which is the scenario for the development of next chapters.

Recalling Fig. 1.2, the LHC circumference is made of eight arcs where the beam trajectories are bent and eight straight sectors that host the interaction regions. Each arc contains 154 bending dipole magnets, giving a total of 1232 main dipoles (MB), accompanied with 392 main quadrupoles (MQ) and many other correctors.

The superconducting niobium-titanium (NbTi) magnets are maintained at a cryogenic operating temperature of 1.9 K thanks to a superfluid helium pumping system. Even a small temperature increase would cause the material to become normal-conducting, which is called a quench. Quenches have to be avoided since the magnetic field cannot be maintained at their occurrence, causing the operation to stop: the beam has to be dumped and a new beam has to be injected, which takes a few hours–i.e., precious time lost for collision.

Superconducting magnets must then be protected from the energy losses coming from the beam. Let us recall that the total energy stored in a 7 TeV beam of the LHC reaches 362 MJ. The absorption of a derisory fraction of this energy could cause a superconducting magnet to quench (see sec. 2.1 for more details on limit losses allowed to prevent quenching). Beam loss monitors (BLM) are installed to control the beam induced losses and if necessary they can trigger the beam dump in case of high quench risk.

Nevertheless, major beam losses risk also to damage sensitive equipment and accelerator components, which must be protected too.

With a view to performing safe and efficient operations, it is of great importance to ensure an effective beam cleaning in order to prevent beam induced losses. This task is performed by the collimation system. Two insertions are dedicate to betatron (IR7) and momentum (IR3) cleaning, thanks to the installation of several collimators that catches particles from the beam halo (See useful references: [4, 27, 28]).

Collimators are made by two movable jaws with an active part from 60 cm to 1 m

long (but some are made by one jaw alone). The jaws are installed parallel to the beam inside the pipe aperture, and the collimator half-gap is given by the distance from the beam orbit to the jaws surface. The collimators aperture is normalized in unit of betatron beam size σ.

Collimators usually follow a hierarchical scheme, as shown in Fig. 1.8: the primary collimators (TCP) closest to the beam are made with robust material—i.e., carbon fiber composite (CFC)—in order to intercept the energetic primary beam halo. The scattered particles form the secondary halo, which must be intercepted downstream by secondary collimators (TCS) with larger half-gap, made with CFC too. Active absorbers (TCLA) are present further out. Tertiary collimators (TCTs) made with tungsten (which has a much higher stopping power but is more fragile) protect the aperture bottleneck at the experiments. Dump protection (TCSP and TCDQ) is installed in IR6. Warm normal-conducting magnets (without any risk of quenching) are used in the cleaning insertions, where losses and secondary showers cause higher energy deposition than in other parts of the ring.

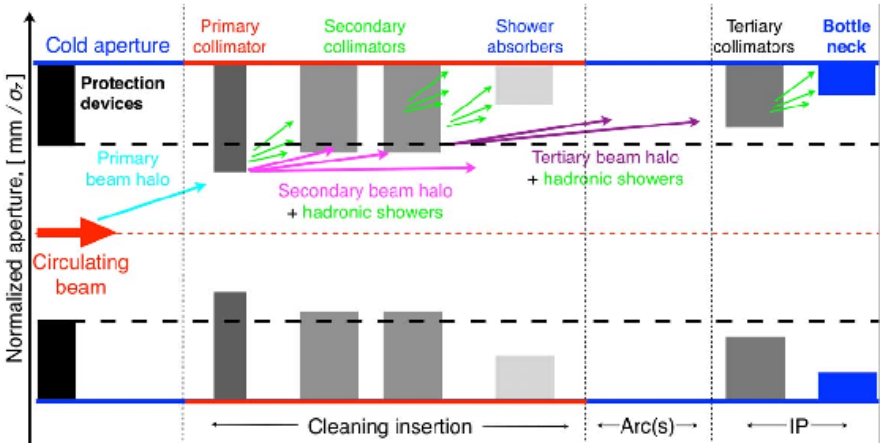

FIGURE 1.8: From [28]. Key elements of the LHC multistage collimation system at an IP.

All the cold magnets must have larger aperture than the collimation system. Typical bottlenecks are the the inner triplet magnets in the final focusing system of the experimental IRs: decreasing β^* to gain luminosity causes the β-function to increase in the triplets, which means that the normalized magnet aperture becomes small. The TCTs need then to be closed in for safe operation. As an example, in Fig. 1.9 a schematic view of the magnets and collimators in the ATLAS insertion (IP1) is shown.

Collimation plays a role also in cleaning collision products with installations downstream the high-luminosity experiments. Moreover, beam tail scraping or local shielding at the detector locations can reduce spurious signals in detectors optimising the experimental background.

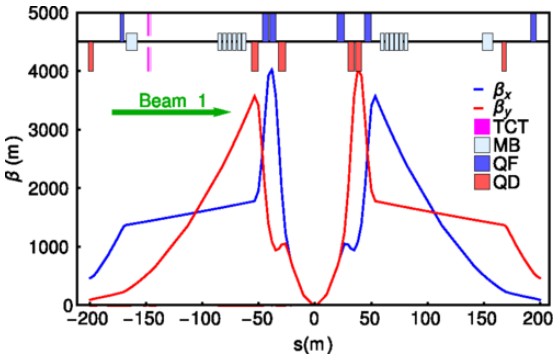

FIGURE 1.9: From [27]. The β-functions around the ATLAS experiment in the LHC for the B1, calculated with mad-x (see sec. 2.2.1) from the optics of 2012 physics run ($\beta^* = 60$ cm), shown together with the layout of dipoles (MB), horizontally focusing (QF) and defocusing (QD) quadrupoles, and tungsten TCTs for protection of the aperture bottleneck. The IP is located at s = 0 and the beam direction is from left to right, meaning that the incoming beam passes the TCTs before the inner triplets and the IP. The optics is identical in CMS except that the horizontal and vertical planes are switched.

1.5 Feasibility Issues

The installation of a gas target at the LHC for parasitic scattering experiments requires extreme carefulness from the point of view of operational safety and compatibility with the normal activity schedule of the LHC. Indeed, it is essential to work in the direction of minimizing the impact on the LHC experiments and on the LHC machine.

To this aim, the PBC-FT group is addressing to some points that need to be carefully evaluated. Details from the various fields have been collected in the report [14]. The evaluation of these effects may limit the allowed target thickness, or even jeopardize the whole feasibility of the implementation.

Among the highlights there are studies on:

i. compatibility with the vacuum system and on dynamic vacuum effects, related to the performance of the SC mechanism described in Section 1.2.1.2;
ii. impact on beam life time and luminosity reduction in the colliding beam experiments;
iii. impact on machine safety in terms of beam losses induced by beam-target collision.
iv. wake field and impedance effects (local heating and beam instabilities);
v. aperture limitations for the SC;
vi. predictions on the background induced on the host experiment and other experiments.

The strong interest in installing a SC at the SMOG upgrade during Long Shutdown 2 has given a push to these studies, consolidating a synergistic work between the PBC-FT working group and the SMOG collaboration. Let us recall that SMOG2 is going to operate in Run 3 of the LHC, while the PBC experiments look to the HL-LHC era. This difference has implications on most of the listed points.

This thesis work addresses point iii. and v. of the list, that will be treated in two

parts: the first one concerns the impact of losses from beam-gas interactions around the ring, and the second part describes studies to determine the allowed minimum aperture of the storage cell.

In Chapter 2 it is reported the study of the impact of beam-gas interaction on the machine safety and the overall LHC program, with respect to particle losses. Indeed, the impact of a 7 TeV proton beam on the gas target under study, is expected to release interaction debris and scattered products that could strongly deviate from the beam orbit and energy. A detailed study of their behavior is needed to check the impact of these products on the experimental equipment. The target density could be reduced if needed. This study is reported in ref. [29, 30]

Finally, as it was explained in Section 1.4, all the elements installed inside the accelerator pipe must be protected by the collimation system. Indeed, the SC is not exempted from this safety measure. This puts limits on the minimum acceptable cell aperture, which are studied in the final part of this work (Chapter 3). This study is reported in the CERN note [31].

CHAPTER 2

Study of beam-gas interaction

The purpose of this work is to study in detail with accurate simulations the beam losses produced by beam-gas interactions in a gas target placed few meters upstream the LHCb detector at IP8 (with respect to B1 reference system). A prediction of the magnitude and precise location of the beam losses along the beam line is needed in order to check if the losses could threaten the sensitive machine equipment, locally or somewhere in the line.

The interaction of a 7 TeV proton with a target atom is a complex process that can give rise to a multitude of secondary particles, since different kinds of interactions come at play. Our studies are based first on realistic simulations of the beam interactions on the target, followed by the debris tracking along the LHC lattice with losses recorded.

In this work, elastic and inelastic scattering interactions are treated in separate simulations, and the most important contribution in term of particle deviation and losses is expected to come from the inelastic case. As it was explained in Section 1.2.1.2, the target SC is designed to host several gas species, with atomic weights ranging from molecular hydrogen to xenon. The beam-gas interaction cross section scales with the gas atomic weight, meaning that we expect a higher interaction rate for heavier elements. On the other hand the resulting deviations in angle and energy are expected to be larger for interactions on light elements. Therefore, the simulations are performed for H and Xe targets as limiting cases with atomic areal density $\theta = 10^{14}$ atoms/cm^2, and the other gas species are expected to lie in-between.

Since the target position was not yet definitely established, simulations of inelastic interactions were repeated for two cases: the target centre was put at either -1.5 m or -3.0 m upstream from IP8, in the B1 reference system. In this way, any dependence on the target position can be evaluated.

The simulations for inelastic interactions, for both target locations, were repeated also for Beam 2. Actually, the target location falls in the region of merging of the two beam pipes, so that both the beams are expected to cross it. Indeed, while the scattering products from B1 are the most relevant from the point of view of the experiment, the scattered particles from both the beams could represent an issue for the equipment nearby.

Finally, the energy loads on cold magnets resulting from the simulations need to be compared with the magnet quench limit that we have already mentioned in Section 1.4. In the cases where that value was exceeded, the target density could be scaled to assure safe operations.

2.1 Quench Limit

Let us briefly explain what is the quench limit and how is it determined. Details on this topic can be found at [32].

The energy of a proton impacting on matter is dissipated either generating hadronic showers (which ignite electromagnetic showers from the β-decay of pions), or via ionization of the target atoms. In both cases almost all the energy is converted to heat, because the produced electrons transfer their kinetic energy to the lattice or emits photons that are reabsorbed by the lattice and transformed into phonons. These possible interactions have been simulated in order to understand the shower development through a model of the complex structure of the LHC magnet superconducting coils. In this way, the maximum energy density deposition per proton per meter was evaluated. This gives for protons at top energy (7 TeV): $E_{dep} = 4.0\ \mathrm{GeV\,m\,cm^{-3}}$ [32].

In the case of a continuous heat deposit on the magnets, which would be the case for beam particles continuously scattered within the internal gas target during normal physics operations at top energy, it is needed to have a continuous evacuation of heat to keep the temperature constant in the cables, and below T_c at which the transition starts from super- to normal conduction in NbTi alloy. The limit of heat flow is set by the conduction of heat by the cryogenic helium flow through the insulation of the coils. The peak power deposition that can be tolerated (with sufficient heat evacuation) without quench by a dipole is $\omega_q = 5\ \mathrm{mW\,cm^{-3}}$. The number of protons which can be lost locally per second in a continuous way must therefore be less than the limit:

$$\dot{n}_q = \frac{\omega_q}{\epsilon} = 7.8 \times 10^6 \mathrm{p\,m^{-1}\,s^{-1}}. \tag{2.1}$$

This limit was assumed during the LHC design to assure operation safety. Multiplying the particle rate per unit length by the proton energy, the limiting power loss per unit length is found, i.e., 8.75 W/m.

It is known today that this quench limit is rather conservative, and quench limits measured with beam are a factor of a few higher [33]. The quench limits show also a dependence on the exact impact distribution on the beam screen, which requires dedicated simulations in several steps and is not realistic to study in detail for the loss location in this thesis. In order to introduce a safety margin, and to compensate for

uncertainties in the distribution, we assume conservatively the LHC design quench limit in this work.

2.2 Simulation Tools

The simulations described hereafter were performed by adopting simulation tools that are routinely used in the context of the collimation and machine protection studies. Let us briefly describe the general features of the two main codes involved, SixTrack and FLUKA, and their coupling. An example will follow of simulation and measurement of beam loss pattern in regular cleaning conditions at the LHC. Details on how simulations and measurements of beam loss patterns are performed at the LHC can be found at [34].

2.2.1 SixTrack

The single particle tracking code SixTrack [35, 36] is one of the most speed optimized computing codes for tracking particles. It is based on thin-lens element-by-element tracking in the six-dimensional phase space, using transfer matrices to describe the effect of each lattice element on the beam. It considers the non-linear magnet component up to order 20. In this way, particles can be tracked over a large number of turns taking into account all relevant imperfections, linear and non-linear fields, beam-beam kicks, and other errors for the accelerator. It was originally conceived to perform dynamic aperture calculations, and it was extended for the tracking of large ensembles of halo particles taking into account the interactions with collimators.

The sequence of magnetic elements taken as input by SixTrack can be generated by MAD-X, a general-purpose tool for charged-particle optics design and studies in alternating-gradient accelerators and beam lines [37]. A detailed aperture model with 10 cm longitudinal precision is also provided as input to SixTrack.

When a tracked particle is found to hit a collimator, the outcome of the interaction can be simulated with different codes, either an external instance of FLUKA (see Sec. 2.2.3) or a built-in Monte Carlo code [38]. Multiple Coulomb scattering, Rutherford scattering, nuclear elastic and inelastic scattering and single diffractive events are considered. The energy loss is recorded and if the proton survives the passage through the collimator material it re-enters the beam vacuum for tracking further. The particles hitting the aperture are recorded as lost.

SixTrack outputs provides a detailed recording of aperture losses, with the coordinates and energy corresponding to each loss. The plot of the losses as a function of the longitudinal coordinate s is called a "loss map". The efficiency and versatility of this code have made it the main tool for simulating the cleaning of the collimation system in the last decades. It is used for example to study in detail new machine configurations in order to respond to the most varied LHC schedule necessities.

Usually, to save computing time, it is rarely given a full beam as initial distribution for the simulation. Typically, each simulation tracks a few 10^6 halo particles over 200 turns. The halo distribution is obtained sampling the coordinate phase space, and many possible distributions are available. Typical options are flat distribution in the

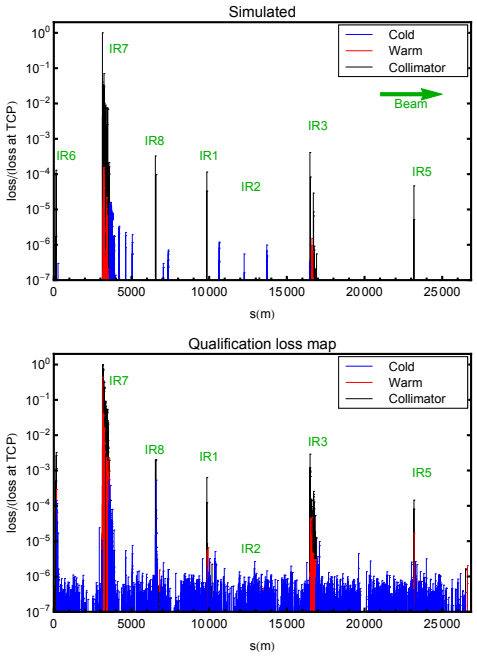

FIGURE 2.1: From [34]. Beam loss distributions around the LHC as measured by BLMs during a qualification loss map on April 12, 2011 (top) and from a SixTrack simulation (bottom). Bin width: 1 m. It is assumed a beam energy of 3.5 TeV and $\beta^* = 1.5$ m. They are both normalized to the highest loss, and the initial losses occur in the horizontal plane in B1. The s coordinate plotting starts from IR6.

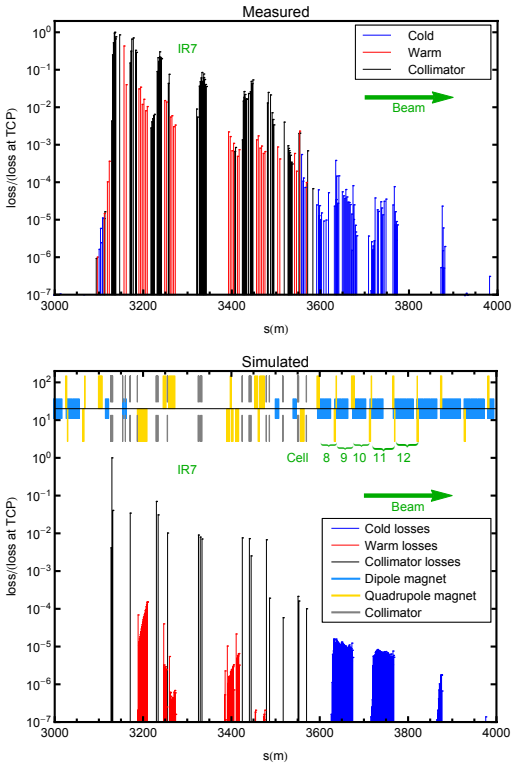

FIGURE 2.2: From [34]. Zoom of Fig. 2.1 on IR7: loss locations from measurement (top) and SixTrack (bottom). The layout of the main magnetic elements (quadrupoles and dipoles) as well as the collimators is also shown, together with the LHC cell numbers at the cold loss locations.

selected (horizontal or vertical) plane around a normalized amplitude that matches the TCP half opening: $A_{x(y)} \pm \delta A_{x(y)}$, while on the other plane one samples either a zero amplitude or a Gaussian distribution. Other possibilities are flat distributions in both planes, or custom six-dimensional external distributions, etc.

The diffusion process that brings halo particles up to the amplitudes needed to hit the TCPs is not simulated. The computing time needed to track the core as well, including diffusion, would be orders of magnitudes longer. Moreover, although we know most of the effects responsible for the particle diffusion, there may be others that are not fully understood and quantified. Instead, it is made an assumption on the TCP interception of the halo–and therefore on the diffusion speed–which is reflected in the initial sampling.

To make a practical example, we report the comparison between a measurement and a simulation loss map as can be found in Ref. [34]. In Fig. 2.1 two example loss maps are presented. The top one is plotted from the measurements of BLMs, while

the bottom one represents the corresponding SixTrack simulation. In Fig. 2.2 the corresponding loss maps zoomed in IR7, where the most significant losses are recorded, which is desirable since in IR7 the betatron cleaning insertion is located. Apparently, the agreement might look bad, in particular the simulation seems to underestimate the effective losses. However, it must be taken into account the fact that the simulations show the impacts of primary protons on the beam screen, while measurements show the measured secondary showers outside of the beam line elements. Since two different quantities are compared, we cannot expect a perfect agreement. In fact, BLMs intercept showers from upstream losses as well, which smear out the measured distributions in Fig.2.1. To have a full comparison, one has to simulate the showers caused by the incident protons and the resulting BLM signals.

The simulated loss map in Fig. 2.1 was obtained tracking a so-called *annular halo* in the horizontal plane for B1. It is generated at the start of the LHC in IR1 in order to obtain a matched phase space in the horizontal collimation plane populated uniformly in a thin hollow ellipse, whose thickness covers the normalized betatron amplitude corresponding to the TCP half opening.

Notice the loss distribution on the collimators in the betatron cleaning insertion: the first highest spikes correspond to the horizontal, vertical and skew TCP7s, followed by the TCS7. Red spikes highlight the presence of the warm magnets. After the last IR7 collimator, the blue spikes reveal the presence of cold magnets at the beginning of the arc. These cold losses are clustered in three regions, corresponding to the maximum values of the dispersion function D(s), which induces the off-momentum particle oscillatory motion (remind eq. 1.21).

2.2.2 FLUKA

Besides the tracker, the other simulation code that was used for the purpose of this work is FLUKA [39, 40], a general purpose Monte Carlo code for calculations of particle and ion interactions with matter and transport. The code covers a variety of applications and is updated with state-of-the-art physics models. As an example, with regard to elastic scattering, it exploits tabulated nucleon-nucleus cross sections, while for simulating hadron-nucleus inelastic nuclear scattering, a mixture of tabulated data and parameterised fits based on available experimental data is used.

The user can choose from a variety of beams and target materials and set a customised initial energy. The tracking of particles is performed through a 3D geometry with detailed material composition defined by the user. Primary particles are tracked together with the secondaries created in hadronic and electro-magnetic cascades.

This code is usually used to simulate BLM response to particle showers. In this work, FLUKA was exploited for simulating the primary beam interaction with the gas target with a customized source.f routine.

2.2.3 FLUKA-SixTrack coupling

Part of the simulations of this work were performed thanks to a coupling of the codes previously described. The FLUKA-SixTrack coupling code [41, 42] allows an active

exchange of tracked particles between the two codes and on-line aperture check: particles are tracked by SixTrack through the magnetic lattice, and when they hit some labelled sections like collimators or internal targets, they are transferred to FLUKA. FLUKA simulates the particle interactions with a 3D model of the machine element that was hit. Surviving particles are sent back to SixTrack and tracked further.

During the course of the study reported in this work, an extension to the FLUKA-SixTrack coupling was under development allowing to implement a FLUKA insertion corresponding to an internal target. This beam-target interaction simulation feature perfectly suited our needs, and these studies were thus used as a first application of the new implementation.

2.2.4 A Standard Betatron Cleaning Loss Map

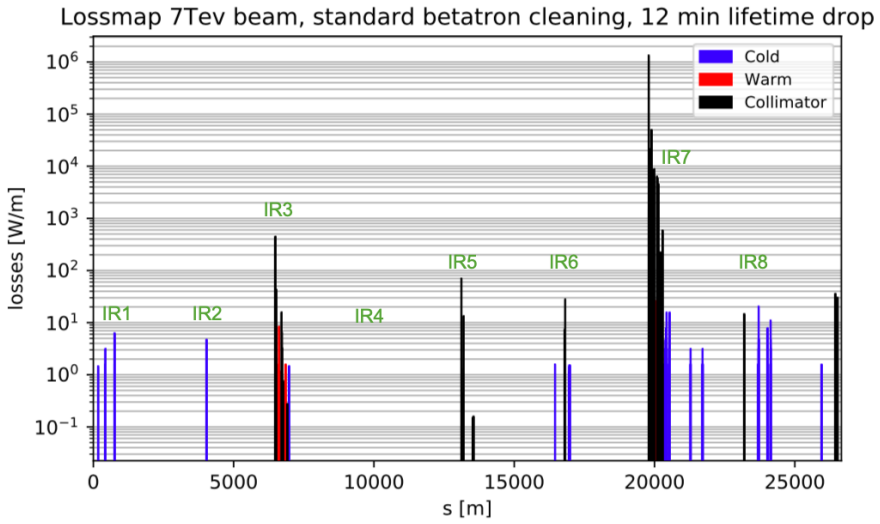

FIGURE 2.3: Beam loss distribution around the LHC for 7 TeV Beam 1, standard betatron cleaning, 12 min lifetime, assuming the HL-LHC beam parameters and a horizontal halo. No interaction with gas targets is included. The maximum cold loss is found to be 20 W/m at s = 23708.2 m. Bin width set to 10 cm. s coordinate starts at IR1.

Fig. 2.3 shows an example of a standard betatron cleaning loss map for a 12 min beam lifetime. This corresponds to the most critical scenario of betatron losses that the collimation system has been designed to handle—that is to say, when the beam intensity decays as $N_0 \exp(-t/t_0)$, with $t_0 = 12$ min decay constant and all the particles impacts on the collimators. If the lifetime would be shorter than 12 minutes, there would be issues with too high heat load on collimators, but also the cold losses leaking out of them could be too high, requiring a beam dump.

The simulation was performed assuming the HL-LHC 7 TeV beam parameters (as found in Appendix A). An annular beam halo was made to impact on the primary collimators in IR7, with an analogous simulation method as the one described in Section 2.2.1 that was used for obtaining the bottom loss map in Fig. 2.1.

Please note that in Fig. 2.3 the s coordinate is plotted setting s = 0 at IP1. The beam travels from left to right. The loss absolute values are given, expressed in W/m. The losses on collimators, cold and warm magnets are plotted with different colors. One can see that the highest spike corresponds to the horizontal TCP where all the tracked particles are made to impact. The surviving particles are mostly absorbed within the betatron cleaning insertion, while some others are intercepted in the momentum cleaning insertion. The remaining particles are either intercepted by local protections at the IPs or lost in the aperture.

2.3 Simulation Setup

Different simulation setups were implemented for simulating elastic or inelastic interactions. We are reporting the two cases separately. The elastic case is not expected to be limiting, since the elastic scattering cross section is smaller than the inelastic. Moreover, particles scattered elastically only lose a small fraction of their energy in the target nucleus recoil, and only receive a small angular kick, so that they could in principle remain within a stable orbit. Conversely, during an inelastic interaction, protons may disintegrate producing low-energy secondaries or lose a great fraction of their energy (diffractive event), which means that more local losses are expected. This is the reason why the study of the inelastic case is more extended than the elastic one.

2.3.1 Elastic Interaction

As a first step, a 7 TeV proton pencil beam (i.e., a beam distribution in the phase space with no spread around the nominal values (s, E, x, x', y, y') = (0, 7 TeV, 0, 0, 0, 0)) is forced to elastically interact with a stationary H or Xe target. This is performed thanks to a customized source.f routine implemented in FLUKA. The interaction cross section is calculated by the code for a fixed target density. The density assumed by the code does not matter for the result of FLUKA simulation, since every single particle is forced to collide.

The energy and direction cosines of the outgoing protons are dumped right after the interaction. In Fig. 2.4 a plot is shown of the angular and energy distribution of the scattered protons, normalised to the total number of incident particles. The angular distribution is found calculating the angle θ_z with respect to the incident direction, starting from the direction cosine z'= $\cos\theta_z$ and considering that the angles are small—i.e., $\cos\theta_z \approx 1 - \theta_z^2/2$:

$$|\theta_z| = \sqrt{2\,(1 - z')}, \tag{2.2}$$

In Fig. 2.5 the x' and y' distributions are shown for elastic interactions on H and Xe targets, normalised to the total number of incident particles. Obviously, the distributions are symmetric in x' and y': indeed, no magnetic field was accounted for in the interaction region.

A curious bump structure is observed for the angular distribution of elastic scattering on Xe for small values of x' and y', that is, the interference pattern of hadron-

nucleus nuclear elastic scattering. One does not find this interference in hadron-hadron scattering, which is obviously the case for proton beam on hydrogen target.

One can notice that the final energy distribution (bottom plot of Fig. 2.4) in the case of elastic scattering on H is wider than on Xe. This is due to the fact that the target H nucleus is less heavy than the Xe nucleus, making it easier to recoil.

As a second step, a beam distribution is prepared by random sampling the coordinates in the x–x' and y–y' phase space. First of all, a set of (x_n, x'_n) and (y_n, y'_n) coordinates in the normalised phase spaces is sampled for every proton from Gaussian distributions centered in zero with $\sigma_n = 1$. Then, the so-obtained normalised coordinates are transformed to the non-normalised phase space with the inverse transformation of 1.18:

$$u = u_n \sigma_u(s) = u_n \sqrt{\epsilon \beta_u(s)} \qquad u' = \sqrt{\epsilon/\beta_u(s)}(u'_n - \alpha_u(s) u_n) \qquad (u = x, y) \qquad (2.3)$$

The transformation is constrained by the value of the optical functions $\beta_{x/y}(s)$ and $\alpha_{x/y}(s)$ at the s-location of the target centre, in order to match the actual beam distribution. The effect of energy spread is neglected. The target position is set at 1.69 m upstream from the IP8 in the B1 reference system. The optical functions at that point are calculated with MAD-X for the optics version 1.3 of HL-LHC. The optics parameters at the target position are listed in Table 2.1.

s from IP8 [m]		**-3.00**	**-1.69**	**-1.50**
s from IP1	[m]	23312.3790	23313.6890	23313.8790
β_x	[m]	5.97	3.93	3.73
β_y	[m]	6.00	3.95	3.75
α_x		9.98E-01	5.60E-01	4.96E-01
α_y		9.99E-01	5.62E-01	4.99E-01
D_y	[m]	1.19E-02	9.93E-03	9.64E-03
D_x	[m]	9.72E-03	3.38E-03	2.46E-03
x	[m]	3.45E-04	1.94E-04	1.73E-04
x'	[rad]	-1.15E-04	-1.15E-04	-1.15E-04
y	[m]	-2.00E-03	-2.00E-03	-2.00E-03
y'	[rad]	1.81E-06	1.81E-06	1.81E-06

TABLE 2.1: Optics parameters as generated by MAD-X at three different target position: -3.00 m, -1.69 m and -1.50 m from IP8 in B1 reference system. The middle value was considered while simulating the elastic beam-gas interactions, while the other two were taken into account for the inelastic case. The value of the optic functions are given, together with the vertical and horizontal transverse phase space offsets x, x', y, y'. The offsets represent the closed orbit with zero betatron amplitude, and their values are non-zero because of bumps for crossing angle and separation.

To each sampled proton from the matched beam distribution, we add the offsets in energy and angle due to the beam-gas scattering from a random sampled final-state proton from FLUKA. This way, the initial conditions correspond to an initially matched beam, where every proton has scattered on a gas nucleus.

In Fig. 2.6 and 2.7 the x–x' phase space density plot is shown for a Gaussian 7 TeV proton beam after the elastic interaction with a H and a Xe target, respectively. The distributions in the x–x' and y–y' phase spaces are almost equal. This condition is not true in general: in this particular case, the optical functions are very similar for both the horizontal and vertical coordinate. Fig. 2.8 and 2.9 show the x' distribution normalized over the transverse beam size σ_x. As is seen, in the interaction with Xe nuclei the beam protons receive weaker angular kicks.

In order to save computation time, a cut of the core is applied at this point to the distribution obtained above. The particles coordinates are transformed into the normalised phase space and only those protons are selected which fall outside 5.5 (units of σ) in either the x_n–x'_n or the y_n–y'_n normalised phase space. The resulting beam halo accounts for the particles that are likely to be lost or intercepted by the collimators.

As it was expected, the fraction of protons receiving a kick large enough to hit the collimators or aperture is very small: in the case of H, up to 80.30% of the initial distribution of the interacting particles had to be cut, while for Xe this percentage rises to 99.35%. This discrepancy is coherent with the different angular distribution shown in Fig. 2.4, 2.8 and 2.9. This cut will be taken into account at the time of normalizing the results.

The x' distributions normalized over the transverse beam size σ_x after applying the core cut are shown in Fig. 2.10 and 2.11 (fro H and Xe target respectively). A curious triple-peak structure is obtained, which is explained as follows. Since the effect of the scattering only widens the angular distributions x' and y' (and not the position ones), when the coordinates of the scattered particles are transformed to the normalised phase space, the populated disk is generally broadened, but it's mainly deformed along the x'_n (y'_n) axes, assuming an elliptic shape. Thus, the condition $x_n^2 + x_n'^2 > 30.25$ tends to select those particles populating the regions of the ellipse where $|x'| \gtrsim 5.5$, that are represented by the external peaks in the x'/σ_x. At the same time, some particles in the core of the x_n–x'_n phase space ellipse might nevertheless be selected because they fulfill the condition on the y_n–y'_n phase space. And this explain the bump at the center of the lateral peaks in x'/σ_x. The same applies for y'/σ_y.

The beam sampled with FLUKA has to be large enough so as to get an available halo beam made of 6×10^6 protons after all the manipulations an cuts. The halo beam is given in input as initial custom beam distribution to the SixTrack code implemented with a collimation routine. SixTrack tracks element-by-element over 200 turns along the HL-LHC lattice, starting from the target position, after adding the appropriate nominal orbit offset to the (x, y) coordinates of the initial distribution.

The losses on collimators and aperture are recorded and downloaded, and the output at this point is ready for the analysis that will be described in sec. 2.4.

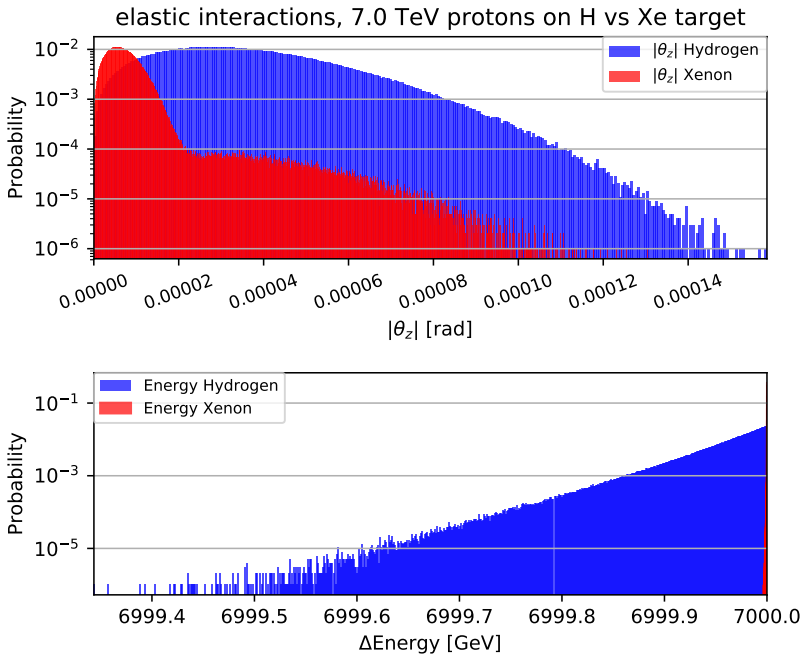

FIGURE 2.4: Distribution of the scattering angle with respect to the initial direction (top) and of the energy (bottom) of 7 TeV protons after facing elastic interactions with H (blue) and Xe (red) target, as simulated with FLUKA. Both histograms are normalised to the total number of incident protons.

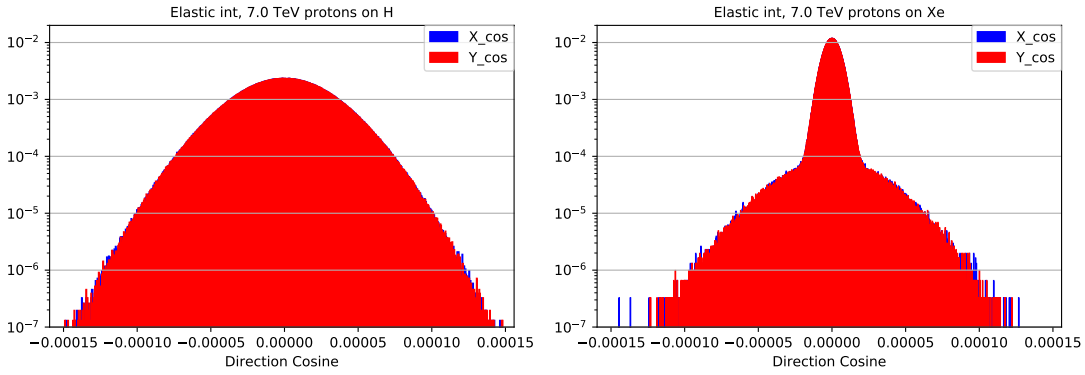

FIGURE 2.5: Distributions of cosine directions in vertical and radial plane for a 7 TeV pencil proton beam after elastic scattering on a H (left) and a Xe (right) target. The histograms are normalised to the total number of interacting particles.

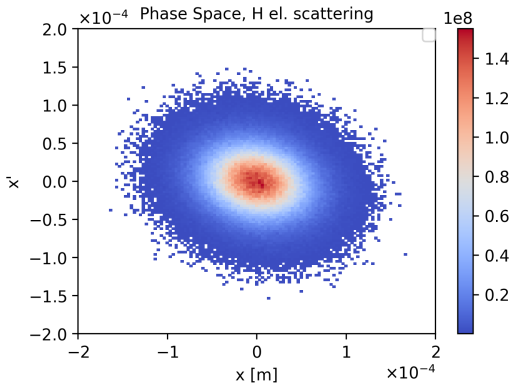

FIGURE 2.6: Beam x–x' phase space density plot for a 7 TeV Gaussian proton beam after undergoing elastic interaction with H target at -1.69 m from IP8 (B1 r.s.). $\sigma_x = 3.63 \times 10^{-5}$ m. The distribution is normalised to the total.

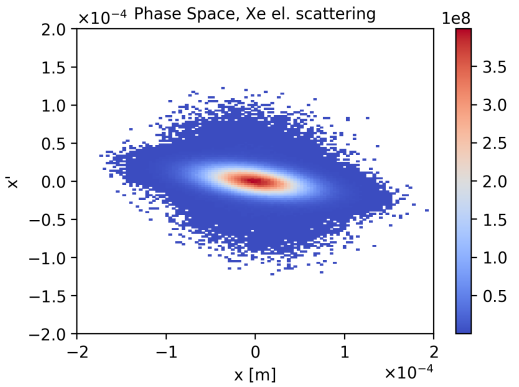

FIGURE 2.7: Beam x–x' phase space density plot for a 7 TeV Gaussian proton beam after undergoing elastic interaction with Xe target at -1.69 m from IP8 (B1 r.s.). $\sigma_x = 3.63 \times 10^{-5}$ m. The distribution is normalised to the total.

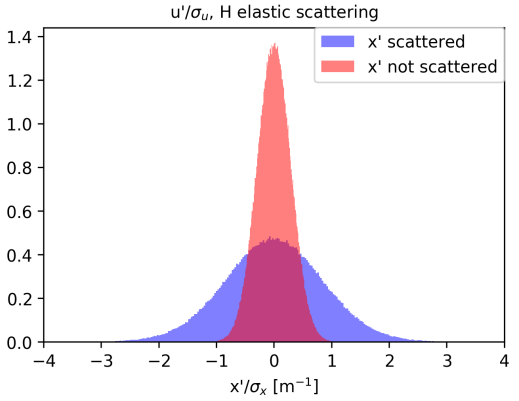

FIGURE 2.8: x'/σ_x distribution for a 7 TeV Gaussian proton beam before and after undergoing elastic interaction with H target at -1.69 m from IP8 (B1 r.s.). $\sigma_x = 3.63 \times 10^{-5}$ m. Normalised to the total.

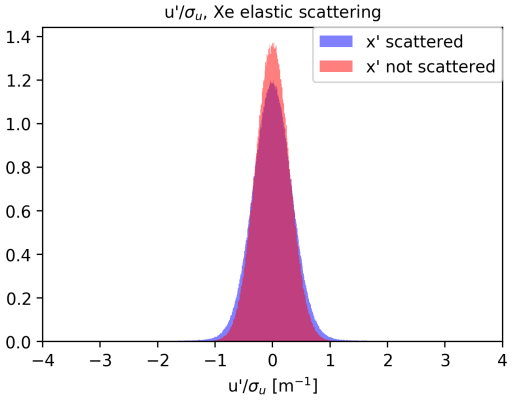

FIGURE 2.9: x'/σ_x distribution for a 7 TeV Gaussian proton beam before and after undergoing elastic interaction with Xe target at -1.69 m from IP8 (B1 r.s.). $\sigma_x = 3.63 \times 10^{-5}$ m. Normalised to the total.

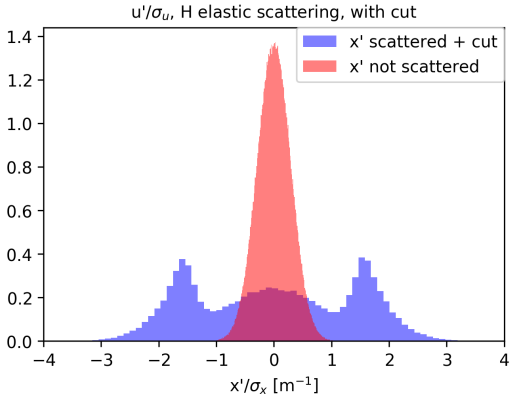

FIGURE 2.10: x'/σ_x distribution for a 7 TeV Gaussian proton beam before and after undergoing elastic interaction with H target at -1.69 m from IP8 (B1 r.s.), with cut at 5.5σ in the normalised phase space. $\sigma_x = 3.63 \times 10^{-5}$ m. Normalised to the total.

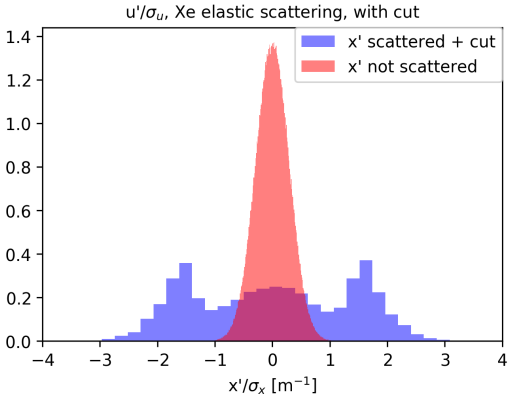

FIGURE 2.11: x'/σ_x distribution for a 7 TeV Gaussian proton beam before and after undergoing elastic interaction with Xe target at -1.69 m from IP8 (B1 r.s.), with cut at 5.5σ in the normalised phase space. $\sigma_x = 3.63 \times 10^{-5}$ m. Normalised to the total.

2.3.2 Inelastic Interaction

The simulation setup for the inelastic interaction case was made somewhat easier thanks to the availability of the FLUKA-SixTrack coupling extension for beam-target interaction described in sec. 2.2.3. This meant the possibility of generating a single initial beam distribution which is autonomously forced to interact with the target and then tracked by the coupled codes. The passage of sampling the intermediate distribution right after the interaction through the target to feed the tracking code is skipped as it all takes place subsequently in a single routine.

The geometry for the beam-gas interaction region insertion, implemented in FLUKA, is given by a dummy pipe with longitudinal length larger than a bunch length and the radius much larger than a bunch radius. It is filled with either H or Xe and centered at the target position. Let us recall that two cases are studied, the target being put at -3.0 m and -1.5 m upstream from IP8 in the B1 reference system, in order to check for any position dependence.

The initial distribution is a Gaussian beam matching the optical functions at the starting point, according to Eq. 2.3. The values of the optical functions are calculated with MAD-X and are listed in Tab. 2.1. The tracking is set to start at the entrance of the target section, the interaction is forced to take place within a 20 cm-long portion of this pipe only at the first turn of the simulation. The length of the interaction portion is chosen in order to represent a likely design length for the storage cell.

An energy threshold of 1 TeV was set for the tracking, meaning that the low-energy secondaries and the particles that lose too much energy are lost. Nevertheless, no energy or rigidity cuts were imposed for the particle exchange between SixTrack and FLUKA.

The simulation output report losses on collimators and aperture, which are analysed following the procedure described in Sec. 2.4. The whole simulation was repeated in total eight times, including cases with both H and Xe targets, both -1.5 m and -3.0 m target position from IP8, both B1 and B2.

In Fig. 2.12 and 2.13 the energy and angular distributions are plotted as dumped right after the interaction for a beam with all initial betatron oscillation amplitudes subtracted, for comparison with the elastic case.

In Fig. 2.14 and 2.15 instead, the x' and y' distributions are plotted, normalised to the beam size σ_x and σ_y respectively, for an initial Gaussian beam. Nominal orbit offsets are subtracted. The plots are reported only for the target at -3.0 m and the other case is very similar.

Only the particles surviving the interactions have been taken into account in the plots described above. Indeed, a large fraction of incident particles are lost within the target itself: this correspond to 45% of the initial beam for H and 52% for Xe. As can be seen, both the energy and the angular deviations of final-state protons cover much wider ranges than in the elastic case. Moreover, differently from what happens in the elastic case, the scattering with Xe has a larger angular spread than H.

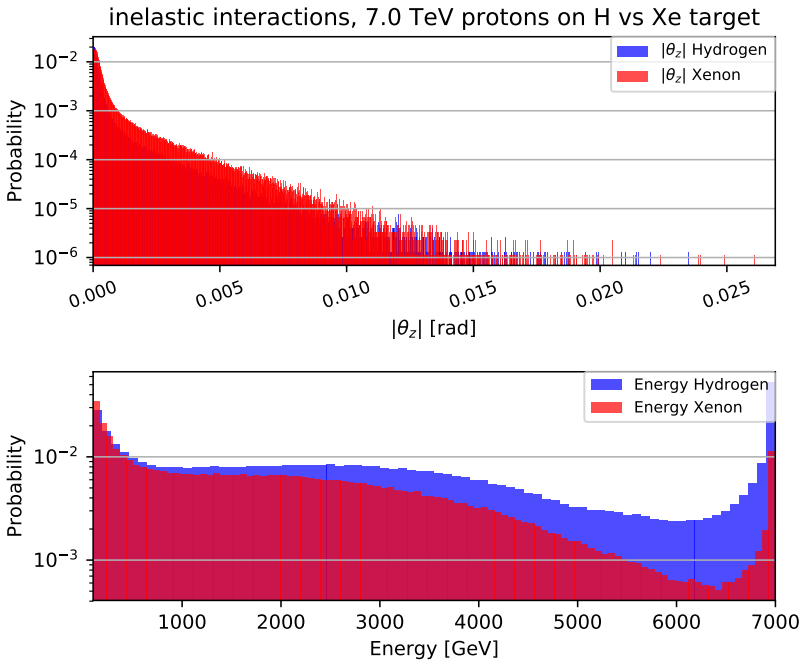

FIGURE 2.12: Distribution of the scattering angle with respect to the initial direction (top) and of the energy (bottom) of 7 TeV protons after facing inelastic interactions with H (blue) and Xe (red) target, as simulated with FLUKA. The histograms only include the protons that did not disintegrate in the interaction (55% of the initial beam for H and 48% for Xe) and are normalised to the total number of incident protons.

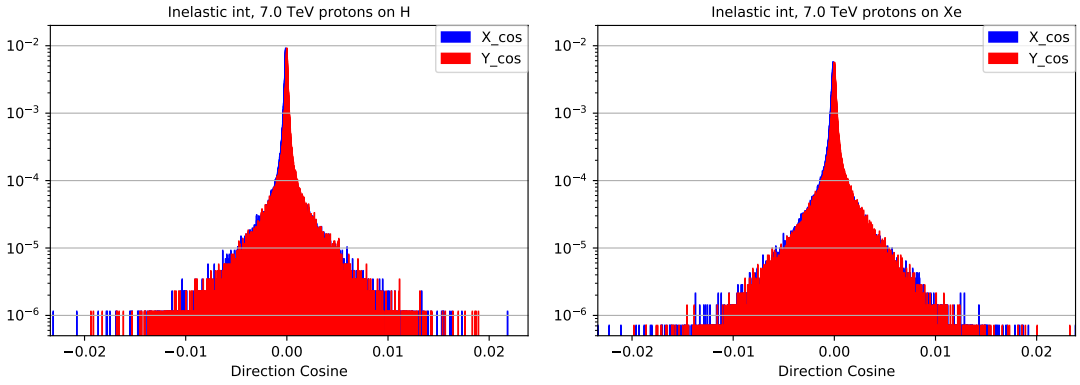

FIGURE 2.13: Distributions of cosine directions in vertical and radial plane for a 7 TeV pencil proton beam after inelastic scattering on a H (left) and a Xe (right) target. The histograms are normalised to the total number of interacting particles.

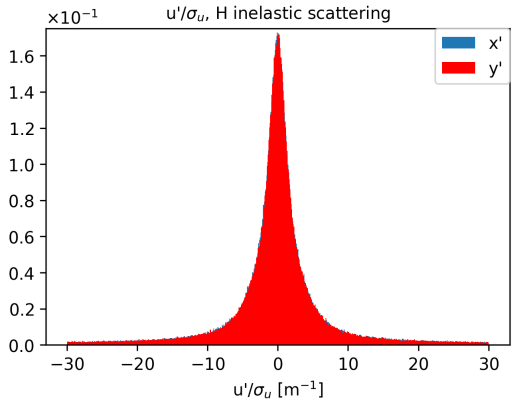

FIGURE 2.14: x' and y' distributions for a 7 TeV Gaussian proton beam after undergoing inelastic interaction with H target at -3.0 m from IP8 (B1 r.s.). σ_x = 4.47×10^{-5} m, σ_y = 4.48×10^{-5} m. Normalised to the total.

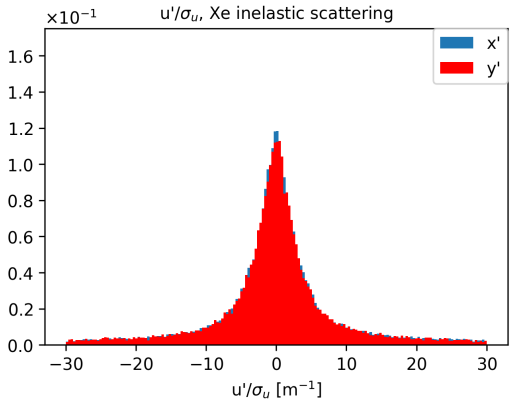

FIGURE 2.15: x' and y' distribution for a 7 TeV Gaussian proton beam after undergoing elastic interaction with Xe target at -3.0 m from IP8 (B1 r.s.). σ_x = 4.47×10^{-5} m, σ_y = 4.48×10^{-5} m. Normalised to the total.

2.4 Data Analysis and Loss Maps Production

The output from the simulations are analysed by plotting the beam losses along the beam line as a function of their s-position. A distinction is made for the losses on cold magnets, warm magnets and collimators. The losses on collimators were recorded separately, since in both simulation routines the particles impacting on the jaws are "extracted" from the tracker for Monte-Carlo simulations. Conversely, the aperture losses (i.e., warm and cold losses) are separated by comparing their position with the subdivision of the HL-LHC circumference into cold and warm sectors.

The loss intensity is expressed in W/m. It is necessary to normalise the losses using the same criteria in order to allow a meaningful comparison. All the loss maps were normalised with respect to the beam-gas interaction rate for the kind of interaction under study. The rate R is calculated as follows:

$$R\ [\mathrm{s}^{-1}] = \text{cross section}\ [\mathrm{cm}^2] \times \theta_{\mathrm{gas}}\ [\mathrm{cm}^{-2}] \times \mathrm{I}_{\mathrm{beam}}\ [\mathrm{A}]/q\ [\mathrm{C}], \tag{2.4}$$

where θ_{gas} is the target areal density and $\mathrm{I}_{\mathrm{beam}}$ is the beam current and q is the proton charge. The beam current is obtained from:

$$\mathrm{I}_{\mathrm{beam}}\ [\mathrm{A}] = \frac{q\ [\mathrm{C}] \times N_b \times n_b \times v_{\mathrm{beam}}\ [\mathrm{m\,s}^{-1}]}{\text{LHC circumference}\ [\mathrm{m}]}, \tag{2.5}$$

recalling that N_b and n_b are the number of protons per bunch and the number of bunches per beam, respectively, while $v_{\mathrm{beam}} \approx \mathrm{c}$ is the beam speed. The parameters corresponding to the version 1.3 of the HL-LHC used for the analysis are listed in Table 2.2.

LHC circumference [m]	26658.8832
primary proton energy [TeV]	7.0
ε_{n} [μm]	2.5
$\mathrm{N_b}$	2.2×10^{11}
$\mathrm{n_b}$	2760
Beam current [A]	1.1
Luminosity at IP8 [$\mathrm{cm^{-2}s^{-1}}$]	2×10^{33}
Cold magnet quench limit [W/m]	8.748

TABLE 2.2: Parameters assumed for the loss map normalisation. Machine and beam parameters are taken as for HL-LHC, version 1.3.

The cross sections and the corresponding event rates for the elastic and inelastic p–H and p–Xe interactions are listed in Table 2.3. The cross sections are calculated by FLUKA for 7 TeV protons, and the interaction rates are derived by taking into account the beam current and the target thickness with Eq. 2.4. The Table lists also the values

		p–H	p–Xe	p–p
	θ_{gas} [atoms cm^{-2}]	1.0×10^{14}	1.0×10^{14}	-
Elastic	Cross Section [mb]	9.0	1000	24
	Interaction Rate [MHz]	6.1	683	48
Inelastic	Cross Section [mb]	38	1408	80
	Interaction Rate [MHz]	26	962	160

TABLE 2.3: Assumed elastic and inelastic cross sections and calculated interaction rates for 7 TeV protons on a H or Xe target at given density. Cross sections and event rates for 7 TeV proton–proton collisions at IP8 are given for comparison. A proton–proton luminosity of 2×10^{33} cm^{-2}s^{-1} is assumed.

corresponding to normal p–p events, for comparison. The p–p interaction rate was calculated taking into account the levelled luminosity at IP8.

The analysis of the simulation results required two slightly different procedures depending on the simulation setups described in Sec. 2.3.1 for the elastic case and in Sec. 2.3.2 for the inelastic one.

In the first case, we recall that the initial beam distribution had to be cut in order to track the beam halo. Moreover, we observe that the protons only lose a small fraction of their energy after the elastic interaction, causing the target nucleus to recoil. As a consequence, it is meaningful to count the losses around the beam line in terms of the number of lost particles. The local number of lost particles is divided by the total number of interactions that was simulated before applying the core cut. In this way, one gets the local losses per interaction event, which are multiplied by the elastic interaction rate, obtaining the local particle loss rates. The local particle loss rate is then multiplied by the initial proton energy and divided by the bin width, in order to obtain the power lost per meter, measured in W/m.

On the other hand, when protons interacts inelastically, the energy distribution of the protons arising afterwards cover a wide range. Thus, in this case it is necessary to consider the local energy losses, instead of the number of lost particles. The same distinction is done when simulating loss maps for ion runs instead of protons. Since the whole beam was tracked with the FLUKA-SixTrack coupling, there are no cuts to account for, and the protons that were lost within the target during the interaction are counted for the normalisation. The local energy losses are divided by the total energy lost along the circumference (comprises the losses within the target), in order to get the local loss per inelastic interactions. The result is multiplied by the inelastic event rate and by the initial proton energy, and divided by the bin width. In this way, the power lost per meter is obtained and it is measured in W/m.

The loss maps in W/m are ready to be compared with the quench limit, which was explained in Sec. 2.1. In the cases where some loss exceeds this safety limit, a re-scaling of the target density has to be foreseen in order to grant safe operations to the experiment. Indeed, the loss intensity is proportional to the interaction rate, which means linear dependence on the gas thickness, according to Eq. 2.4.

2.5 Results

The complete set of the resulting loss maps for beam-gas interaction simulations are reported in this section. The losses on the beam line are plotted from IP1, and the Beam 1 travels from left to right. The plots should be compared with the regular cleaning loss map in Fig. 2.3. Indeed, the losses due to beam-gas interaction have to be considered as superimposed to this regular loss map. The results for the elastic and inelastic case are reported separately, since their contribution is quite different.

2.5.1 Elastic Interaction

Figure 2.16: Beam loss distribution around the LHC, Beam 1 elastic interactions with H (*A*) and Xe (*B*) target at position marked by dashed green line (-1.69 m from IP8). Bin width set to 10 cm.

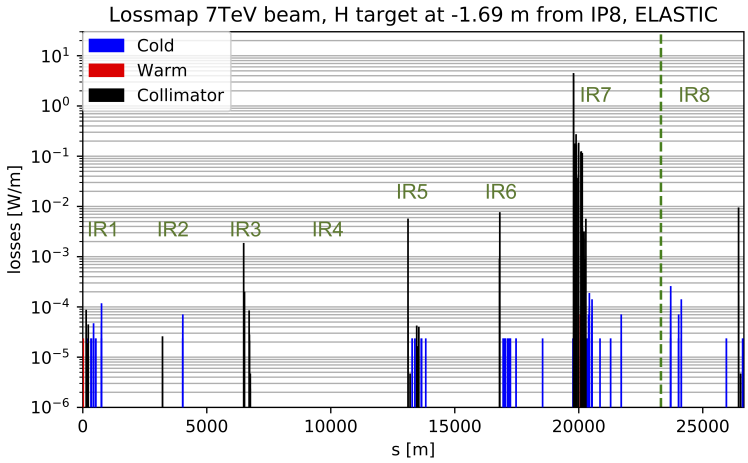

(A) H target at -1.69 m from IP8. Max cold loss: 2.5×10^{-4} W/m at s = 23707.6 m.

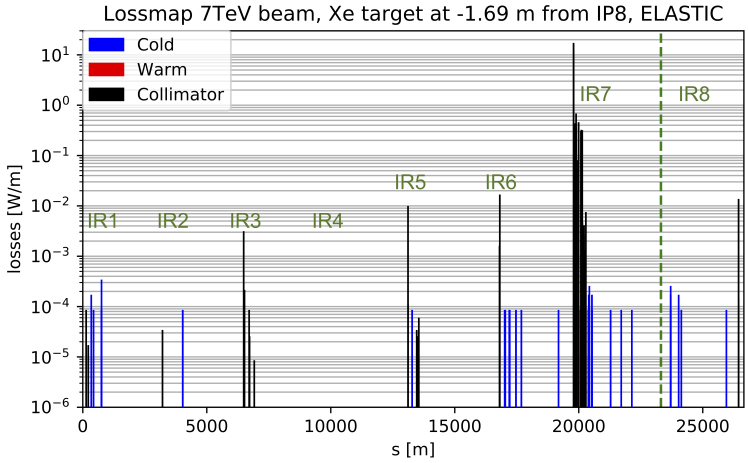

(B) Xe target at -1.69 m from IP8. Max cold loss: 3.3×10^{-4} W/m at s = 755.2 m.

Two loss maps were produced for the study of the elastic contribution to the

beam-gas interaction, corresponding to Fig. 2.16a for H target and Fig. 2.16b for Xe target.

The losses for the elastic contributions are found negligible with respect to the regular cleaning scenario. Moreover, all the cold losses that were recorded are safely below the quench limit. In fact, the highest cold losses reach 2.5×10^{-4} W/m in the H case and 3.3×10^{-4} W/m for the Xe, i.e., five orders of magnitude lower than the quench limit of 8.748 W/m.

No losses are recorded within the target itself, whose location is marked by a dashed green line. This is reasonable, since all the protons survive the elastic interaction without dramatic angular deviation or energy transfer.

Analysing the first impact recorded for every particle lost, it is found that all the lost protons have impacted first on the primary collimators in IR7. This is the usual case for regular beam operation. moreover, the pattern of the black spikes, representing the losses on the collimation system, is very similar to the regular cleaning loss map.

One can conclude that the beam-gas interaction contribution from elastic scattering has no irregular consequences on the behavior of the beam and, most important, it has no harmful consequences for the machine.

2.5.2 Inelastic Interaction

The same conclusion cannot be taken for the study of the inelastic contribution to the beam-gas interaction. The loss maps in Fig. 2.17 correspond to the H target simulations, for the two position cases, while the loss maps in Fig. 2.18 corresponds to the Xe simulations. The results for Beam 2 are reported in Fig. 2.19 for H and Fig. 2.20 for Xe.

The full loss maps come with complementary loss maps zooming into the beam line region going from just before the target to few hundred meters downstream, with respect to the beam under simulation. This region is where most of the losses are clustered. A scheme of the lattice is plotted on top of the zoomed loss maps, showing the main machine elements. Blue rectangles correspond to bending magnets, red to quadrupoles, yellow to sextupoles, light grey to multipoles, purple and pink to horizontal and vertical orbit correctors, and the black lines mark the collimators.

Let us remark the main differences with respect to both the elastic interaction loss maps and the regular betatron cleaning one. First of all, one can notice the presence of a high magenta spike in every loss map, located at the target position. It corresponds to the losses happening within the target itself. As it was explained, indeed, most of the incident protons are lost during the interaction, and many particles have an energy below the tracking threshold, and are thus lost.

Secondly, a higher loss activity is recorded at the momentum cleaning insertion in IR3: the losses recorded there are almost as large as, or even larger than, in IR7. This is due to the presence of strongly off-momentum particles that are intercepted and removed from the beam in IR3.

The losses recorded for the H case are more than a factor 10 lower than in the Xe case, reflecting the different inelastic cross sections. In all the loss maps for B1, the highest loss is found at s = 23553.4 m, on the horizontal orbit corrector MCBCH.6R8.B1

in cell 6 to the right of IP8. In the case of H, the losses are still safely below the quench limit, but the Xe instead causes the limit to be exceeded.

The Xe target thickness should be decreased in order to maintain all the losses below the safety limit. The maximum Xe thickness was calculated to be $\theta_{max} = 1.21 \times 10^{13} \approx 10^{13}$ atoms cm^{-2}. This limit is probably pessimistic. In fact, the quench limit for the orbit corrector magnets is not well known, but it is expected to be less restrictive than for the dipoles. Nevertheless, also the quadrupoles just downstream the target face strong losses, but the quench limit for such magnets is known to be about a factor 2 larger than for the dipoles [33]. The separation dipole D1 (the first dipole following the target) receives almost as high losses as the orbit corrector, and its quench limit is also not well known.

The estimate for the maximum safe target density could be improved by dedicated energy deposition studies for the regions involved, as well as quench limit calculations for the different magnet types. Similar studies were carried on for the High Luminosity proton-proton collision program at LHCb, as reported in Ref. [43]. It was found that thanks to the new TAS and TAN absorbers to be installed for the HL-upgrade, the triplet will withstand a p–p luminosity up to 10^{34} cm^{-2} s^{-1}, which corresponds to an event rate just below the one for p–Xe interaction with a $\theta_{\text{gas}} = 10^{14}$ atoms cm^{-2} gas target. It is hoped that this protection could help also in coping with the beam-gas debris.

We do not find significant differences in losses for different target positions. The loss pattern is almost unchanged, with difference of a few percent on the main losses. Thus, it is concluded that the losses do not depend strongly on the target position within the range under study.

Similar results are found for the B2 simulations. In the loss maps in Fig. 2.19 and 2.20 the beam runs from right to left, meaning that it encounters the target downstream with respect to the LHCb detector. The losses are thus clustered on the region symmetrically opposite from the target with respect to B1 case. The lattice of the region around IP8 is quite symmetric and this reflects almost symmetrically in the loss pattern in the zoomed plots. The highest cold losses are recorded on a quadrupole.

All the maximum cold losses for the inelastic interaction simulations are listed in the summary Table 2.4.

	Beam 1		**Beam 2**	
Target position from IP8 [m]:	**-1.5**	**-3.0**	**-1.5**	**-3.0**
H target, max cold loss [W/m]:	4.1	4.1	2.6	2.6
Xe target, max cold loss [W/m]:	72	72	70	72

TABLE 2.4: Maximum cold losses recorded for simulations of inelastic interaction of a 7 TeV proton beam on the gas target.

FIGURE 2.17: Beam loss distribution around the LHC, Beam 1 inelastic interactions with H target. Bottom plots show details of IR8. Bin width set to 10 cm.

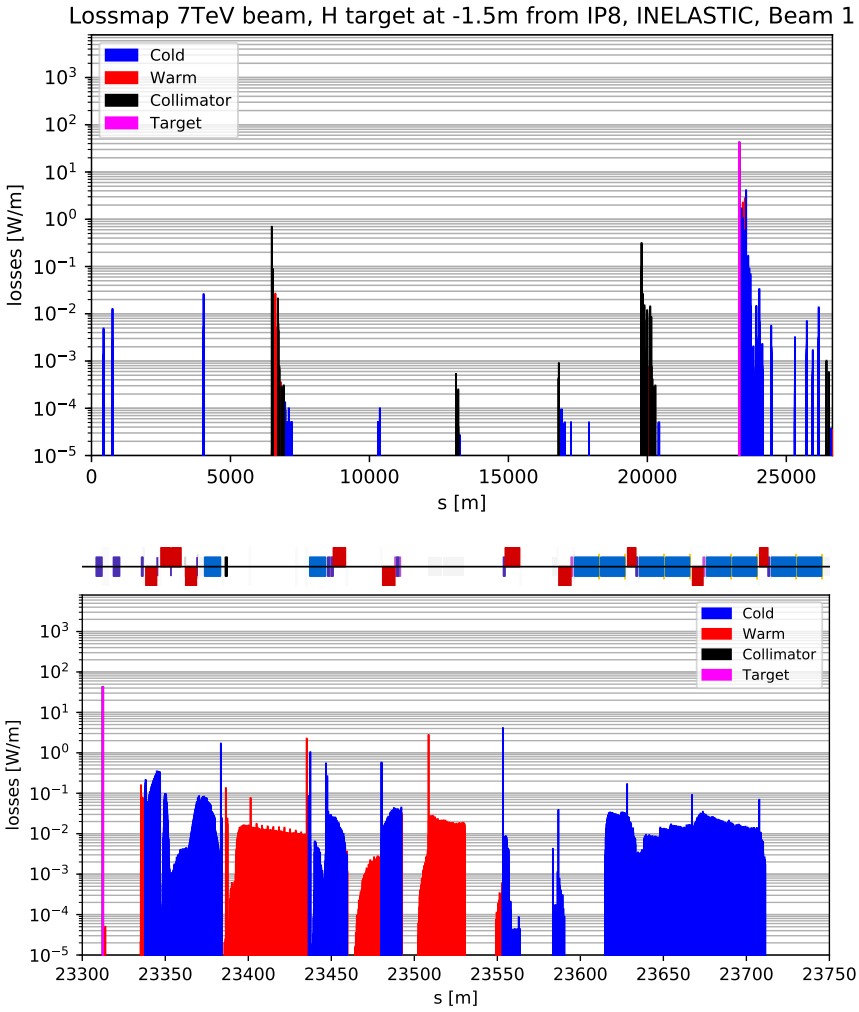

(A) H target at -1.5 m from IP8. Max cold loss: 4.1 W/m at s = 23553.4 m.

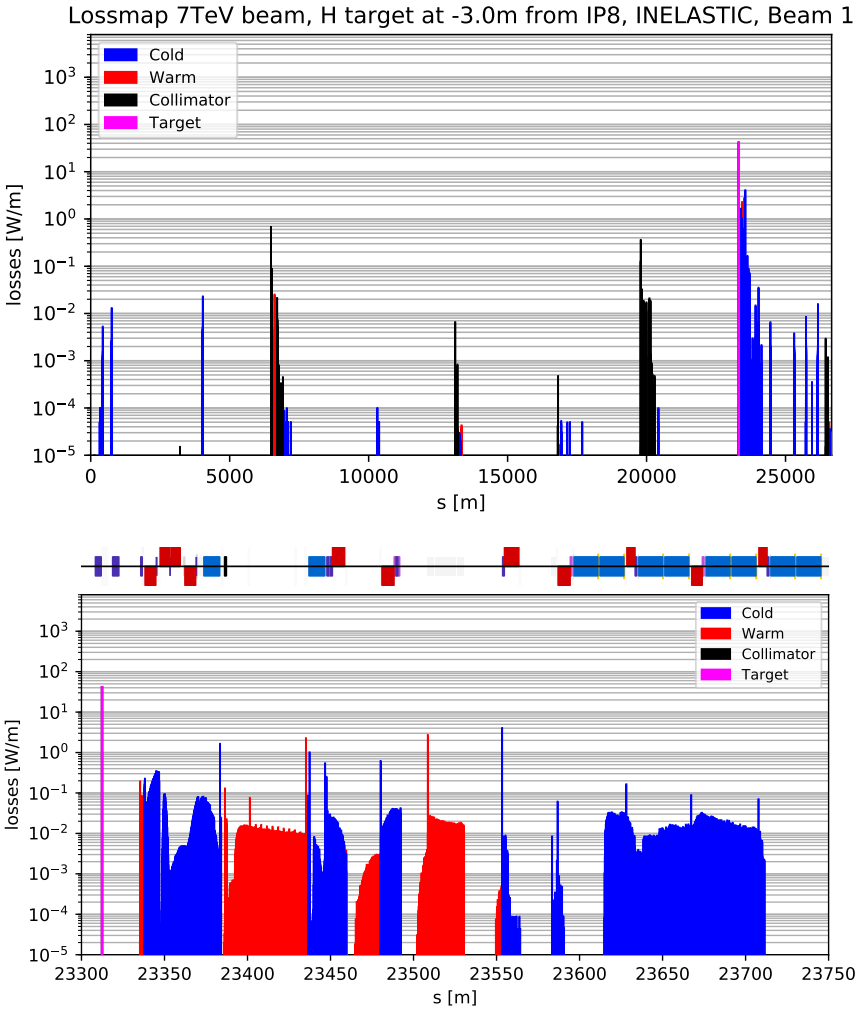

(B) H target at -3.0 m from IP8. Max cold loss: 4.1 W/m at s = 23553.4 m.

FIGURE 2.18: Beam loss distribution around the LHC, Beam 1 inelastic interactions with Xe target. Bottom plots show details of IR8. Bin width set to 10 cm.

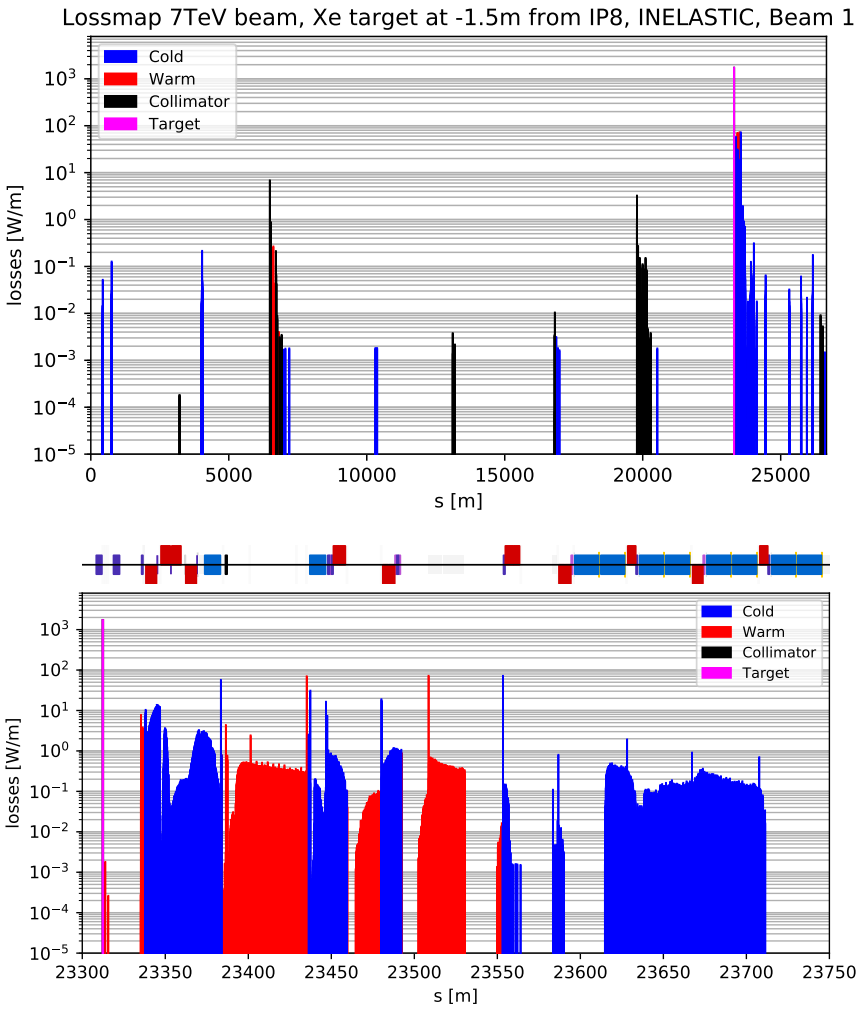

(A) Xe target at -1.5 m from IP8. Max cold loss: 72 W/m at s = 23553.4 m.

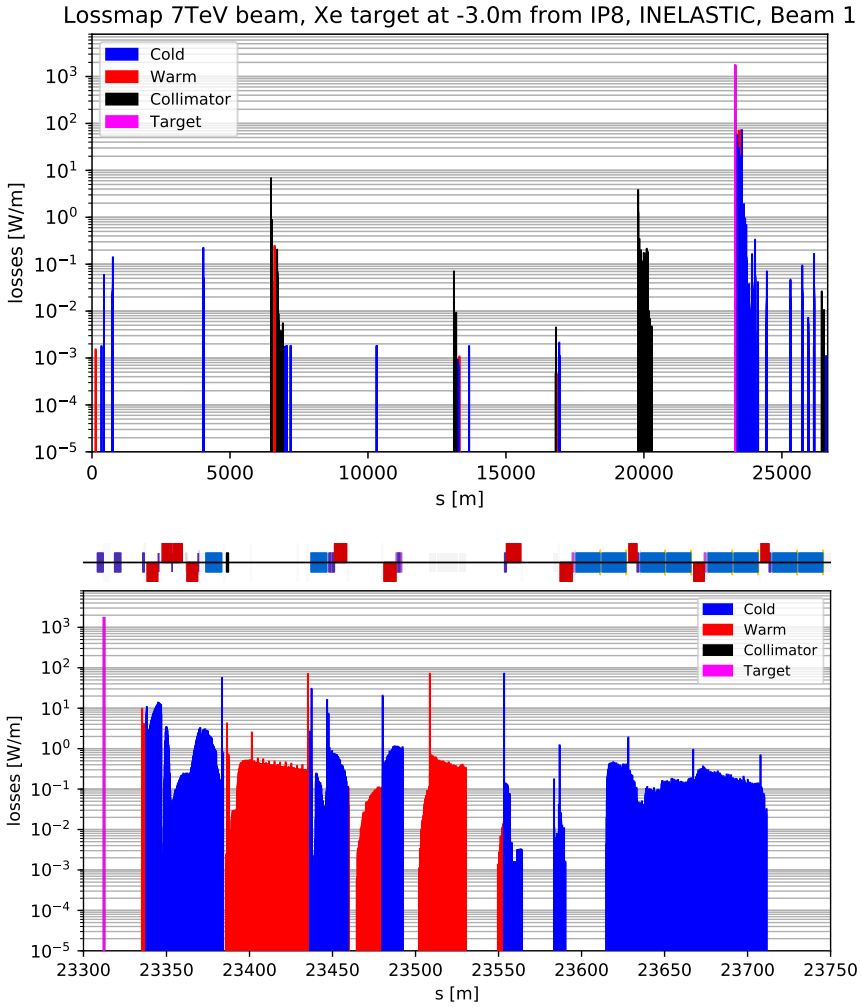

(B) Xe target at -3.0 m from IP8. Max cold loss: 72 W/m at s = 23553.4 m.

FIGURE 2.19: Beam loss distribution around the LHC, Beam 2 inelastic interactions with H target. Bottom plots show details of IR8. Bin width set to 10 cm.

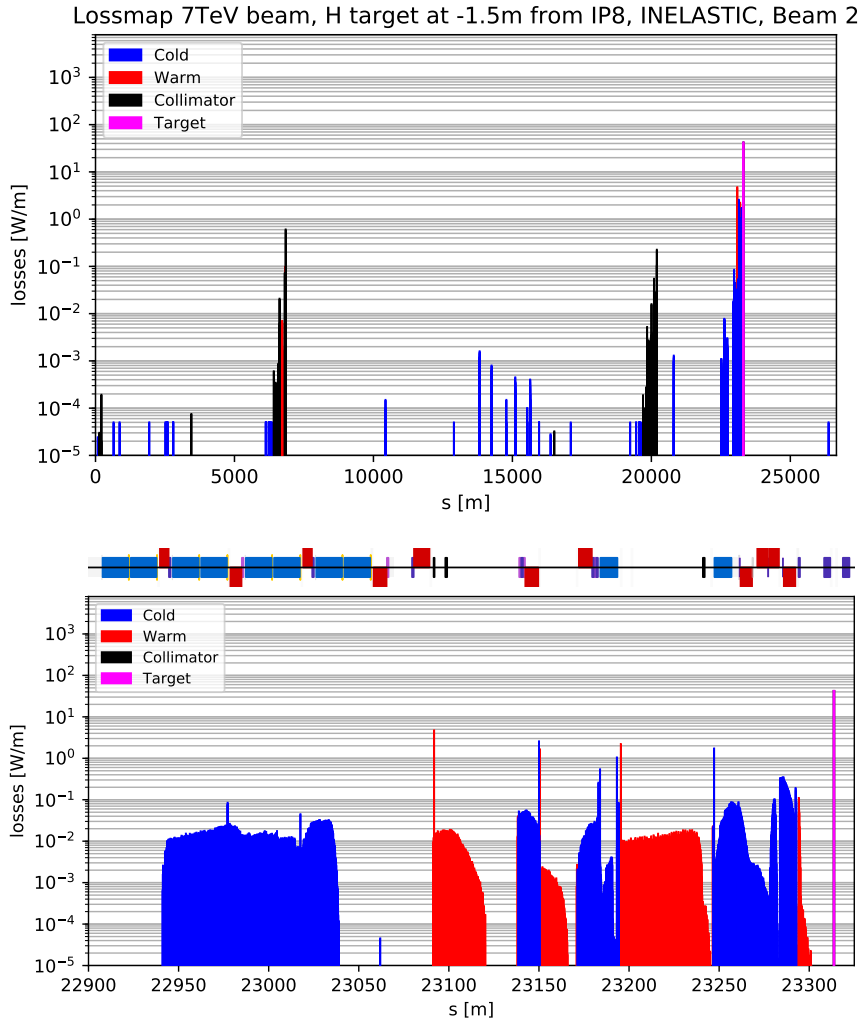

(A) H target at -1.5 m from IP8. Max cold loss: 2.6 W/m at s = 23150.0 m.

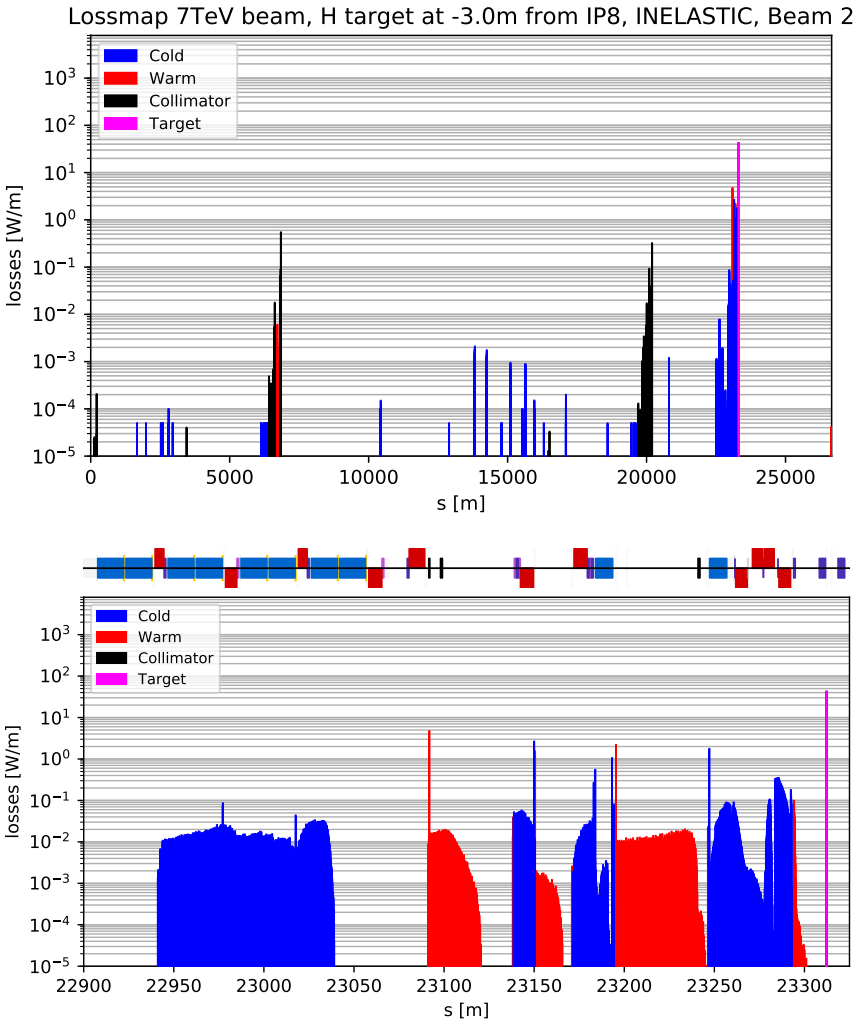

(B) H target at -3.0 m from IP8. Max cold loss: 2.6 W/m at s = 23150.0 m.

FIGURE 2.20: Beam loss distribution around the LHC, Beam 2 inelastic interactions with Xe target. Bottom plots show details of IR8. Bin width set to 10 cm.

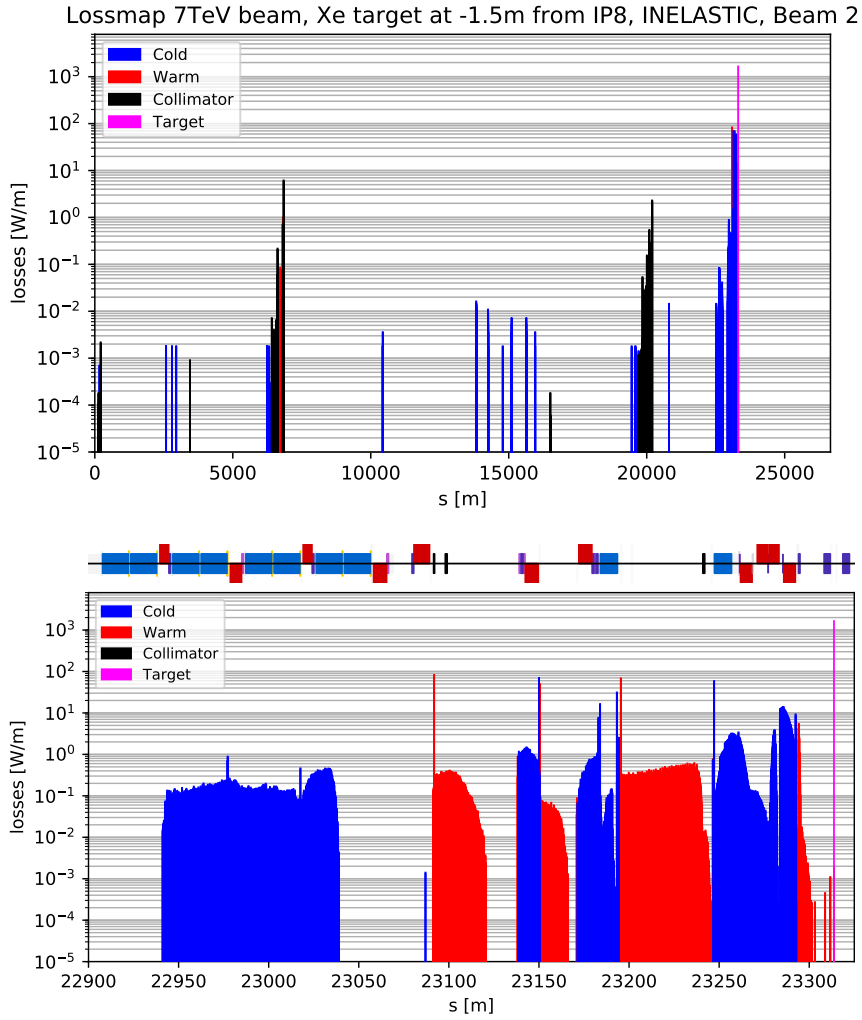

(A) Xe target at -1.5 m from IP8. Max cold loss: 70 W/m at s = 23150.0 m.

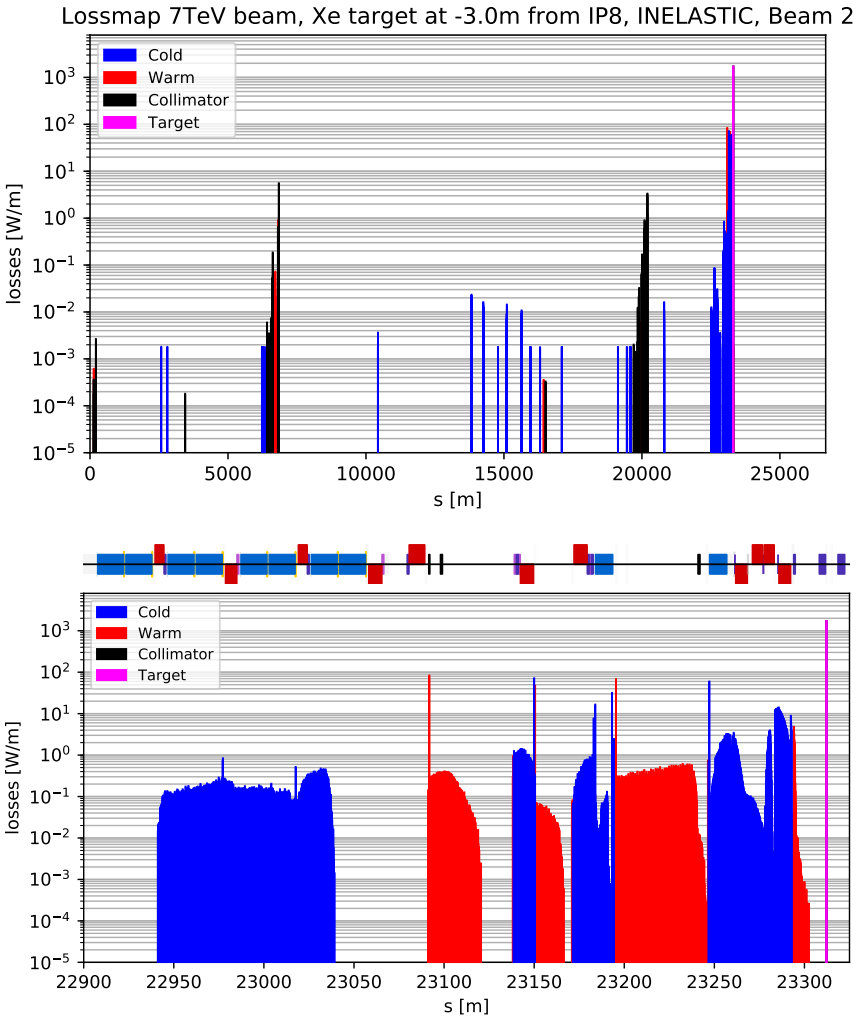

(B) Xe target at -3.0 m from IP8. Max cold loss: 72 W/m at s = 23150.0 m.

CHAPTER 3

Aperture Calculation for a Storage Cell

The second part of this work focuses on the study of the aperture limitation for the SC to be installed at LHCb for containing polarised or unpolarised gas targets. The necessity of this study lies in the fact that when an element is installed inside the LHC pipe, its protection must be ensured by the collimation system in order to grant safe operation. This translates into a minimum acceptable aperture which has to be respected in the design of every element to be installed in the LHC, and the SC implementation for gaseous fixed-target experiment proposal within the PBC study program is not exempt from this constraint. The results of this study are reported in Ref. [31].

First of all, a short recap of the regular machine cycle of a LHC fill is done, followed by considerations on the setup of the LHCb insertion and the luminosity levelling mechanisms. The minimum safe aperture calculation follows, explained in details.

3.1 Operating Cycle and Setup at LHCb

Let us recall that the LHC proton beam is injected at an energy of 450 GeV, with a beam emittance and intensity that show a linear relation depending on the injection system. The beam geometric emittance is larger at lower energy, resulting in a larger beam size. The bunches are injected according to a precise filling scheme, and the usual bunch separation is 25 ns. This phase of the cycle is called the beam *Injection*.

After all the bunches are injected in both rings, the beam energy is progressively increased by the RF cavities through the *Ramp* beam mode, and the current in the superconducting magnets slowly rises such that the beams are always kept on the ideal trajectory. The ramp ends once the protons reach the top energy, and the *Flattop*

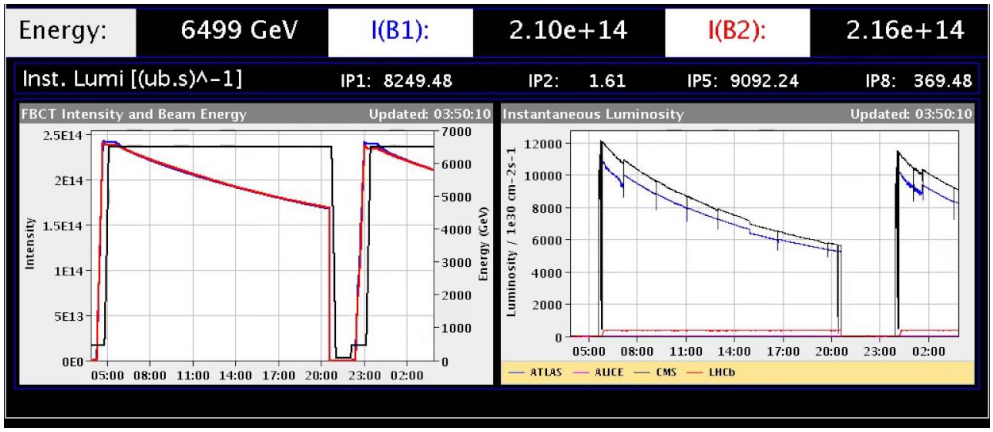

FIGURE 3.1: A representative machine cycle for a LHC fill occurred in August, 28th 2016 with 6.5 TeV proton beams. On the left plot the time variation is recorded of the beam energy (black) and the intensity for B1 (blue) and B2 (red). On the right the time variation is plotted for the instant luminosity at the ATLAS, ALICE, CMS and LHCb IPs.

beam mode is declared. The *Squeeze* of the betatron functions at the collision points is performed either after flattop or along with the ramp, in which case the beam goes through a single phase of combined *Ramp&Squeeze*.

During the *Adjust* mode the beams are brought in collision and then the *Stable Beams* mode begins, where the actual data taking for physics takes place. The duration of the Stable Beams depends on the beam lifetime, which is constraint by the collision rate. When the luminosity falls too much, the *Beam Dump* is set, the beams are extracted from the rings, and the magnet current is progressively restored during the *Ramp Down* mode and the machine is prepared for another cycle.

A scheme of the energy and beam intensity variation during a full fill cycle is shown in Fig. 3.1, together with the correspondent luminosity as recorded at the IPs. One can see that the energy ramp starts just after the full beam intensity has been injected. Moreover, as soon as the beams are colliding at top energy, the beam intensity and luminosity decrease slowly for about 15 hours, after which the beam is dumped and the energy is put to zero again with a ramp down. However, it should be noted that often the fills are interrupted prematurely by beam dumps triggered by the Machine Protection System (MPS) due to equipment faults or other anomalies. In the particular case that is reported, a couple of hours was necessary as turnaround time before establishing a new Stable Beam after the Beam Dump.

It can be noticed that the LHCb detector (represented in Fig. 1.5) works at a lower luminosity with respect to ATLAS and CMS: the luminosity is levelled to 2×10^{32} cm^{-2} s^{-1}. The LHCb is undergoing a major upgrade during LS2 aimed to operating the detector at a constant luminosity (i.e., levelled through every fill) of $\mathcal{L}_{\text{LHCb}} = 2 \times 10^{33}$ cm^{-2} s^{-1} with a 40 MHz readout architecture [44]. This will be the operational luminosity also for the High-Luminosity upgrade [26].

The luminosity levelling is generally achieved at the experiment thanks to a dynamically varying parallel beam separation offset at the IP. These configurations affect

the calculation of the minimum allowed aperture of any element to be installed in proximity to the IP8.

An example of aperture limitation is given by the calculation of the allowed aperture for the LS2 upgrade of the LHCb VErtex Locator (VELO) [45]. This subdetector was introduced in Sec. 1.2.1.1. The VELO is retractable and is only inserted close to the beam during Stable Beams, since the radial distance of the sensors from the beam is smaller than the aperture required by the LHC during injection.

Analogously to the VELO, also the SC that is under study is assumed to be retractable, so that it would be placed at a transverse position centered around the actual beam position only once the Stable Beam is reached. Otherwise, the aperture constraint would be dominated by the beam size at the injection. Nevertheless, several scenarios with colliding beams are taken into account for the calculations, as will be explained in Sec. 3.2.4

The VELO's extent is asymmetric on the two sides of the IP: the downstream edge (according to B1 reference system) extends further from the IP with respect to the upstream one. Thus, any object to be installed upstream IP8 within the mirror projection of VELO's downstream edge, can be considered safe, as long as its aperture is larger than the VELO's, including all tolerances.

3.1.1 Luminosity levelling

Before going on with the description of the aperture calculation, an explanation is given of how the geometrical setup of the IP affects the collision luminosity.

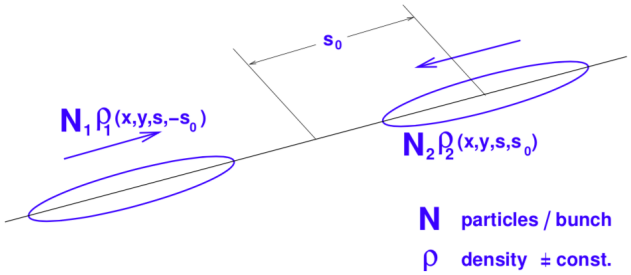

Figure 3.2: From [25]. Head-on collision of two bunches.

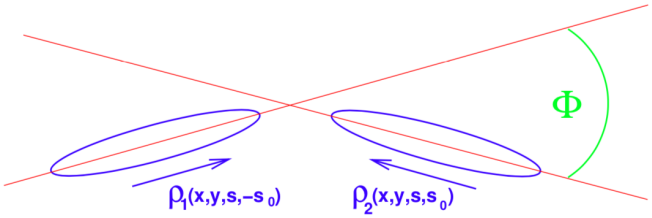

Figure 3.3: From [25]. Collision of two bunches with a horizontal crossing angle Φ.

We said that the luminosity levelling at IP8 is performed by regulating the parallel beam separation. The expression for head-on collision luminosity is given by Eq. 1.24: it refers to collision with no crossing angle and no beam displacement as depicted in Fig. 3.2. When a crossing angle is introduced, the particles from one bunch cross

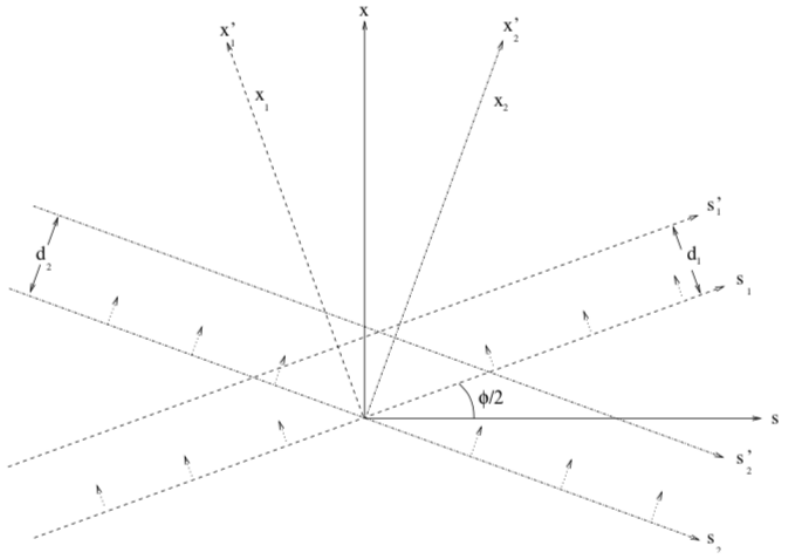

FIGURE 3.4: From [25]. Schematic view of two bunches colliding at a finite crossing angle ϕ and a parallel displacement offset $\lambda = d_1 - d_2$ between the two beams.

transversely the other bunch and the extension of the overlap between the crossing bunches is reduced, as shown in Fig. 3.3: this translates into a lower luminosity. The presence of a parallel beam separation offset further decreases the overlap between the beams and thus the probability of having two protons interacting.

From a mathematical point of view, the exact luminosity calculation is obtained from the overlap integral of the two-dimensional density distribution of the colliding bunches in the x and y coordinates. In order to account for the presence of both a crossing angle and an offset displacement, a proper coordinate transformation is needed, as shown in Fig. 3.4.

The coordinate transformation leads to a new solution to the overlap integral for the case of two beams colliding with a parallel separation offset λ and a crossing angle Φ:

$$\mathcal{L} = \frac{N_b^2 n_b f}{4\pi\sigma_x\sigma_y} \exp\left(-\frac{\lambda^2}{4\sigma_x^2}\right) \frac{1}{\sqrt{1+\left(\frac{\sigma_s}{\sigma}\tan\frac{\Phi}{2}\right)^2}} e^{\frac{B^2}{A}}, \tag{3.1}$$

Where $\sigma_s = 9.0\times10^{-2}$ m is the bunch length, $A = \frac{\sin^2(\phi/2)}{\sigma_x^2} + \frac{\cos^2(\phi/2)}{\sigma_s^2}$ and $B = \frac{\lambda\sin(\phi/2)}{2\sigma_x^2}$, and $e^{\frac{B^2}{A}} \approx 1$ for small angles. The head-on luminosity is thus multiplied by three reduction factors, one depending on the crossing angle, one on the parallel separation and the third on the combination of the two.

We recall that the luminosity is strongly affected by the value of β^*, since it determines the transverse beam size at the IP. Thus, the luminosity calculation is sensitive to any effects on the betatron function, such as beta-beating and the shift of the beta function minimum with respect to IP8, which will be described in Sec. 3.2.3.

3.2 Minimum Radius Calculation

The minimum safe aperture for the SC is calculated as a function of the maximum longitudinal distance reached by the cell with respect to IP8. To this purpose, the transverse plane is considered at an arbitrary s-position upstream of IP8 (according to B1 reference system), and the maximum extent of the beam envelope at this location is calculated as shown in Fig. 3.5. This calculation sets an inner limit to the radius of the SC.

As can be seen in the picture, the centre of the beam is first displaced from the centre of the beam pipe by the total offset $R^{\mathrm{H/V}}$ caused by the foreseen crossing and separation bumps (green dot). Around this point, a random orbit drift due to imperfections is considered (purple circle). The new beam center could be anywhere around the purple circle, and we set it to the most external point (purple dot) in order to consider the largest offset sum. Centred around the new beam centre, the full beam envelope out to n standard deviations (σ) is drawn (blue circle). The three contributions are described in details in the following.

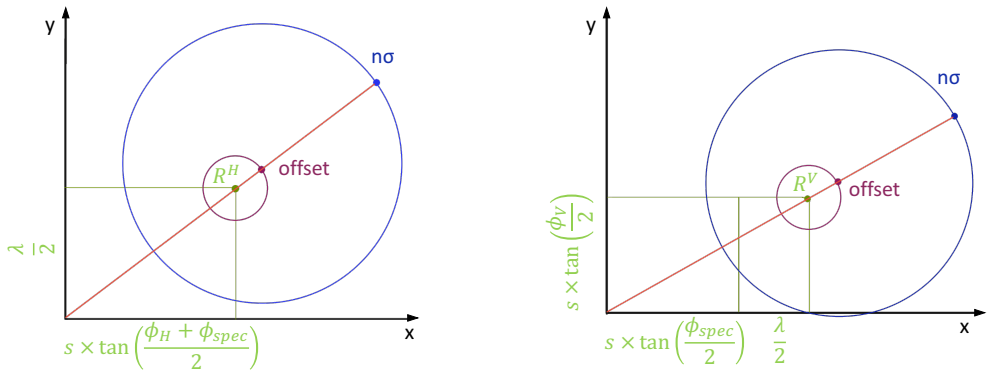

(A) Horizontal crossing configuration: horizontal external angle and vertical parallel separation, summed to the internal horizontal spectrometer angle.

(B) Vertical crossing configuration: vertical external angle and horizontal parallel separation, summed to the internal horizontal spectrometer angle.

FIGURE 3.5: Transverse plane view of the maximum extent of the beam envelope, as constructed for the calculation of the minimum allowed aperture for a SC installed in proximity of IP8. Two crossing configurations are considered. The envelope extent is built by the linear sum of three contributions: the green dots mark the geometric contribution $R^{\mathrm{H/V}}$ given by the beam separation according to the crossing configuration, the purple circles delimit the offset accounting for the orbit drift, and the blue circles delimit the safe admitted margin $n\sigma$ around the beam envelope.

3.2.1 Beam Separation and Crossing Configurations

The standard crossing configuration assumed at IP8 is given by a horizontal external crossing angle ϕ_{H} summed to the horizontal spectrometer angle ϕ_{spec}, which can be set to have either positive or negative polarity (plus or minus sign respectively). In such a configuration, the total crossing angle is fixed and the luminosity must be levelled by

tuning the parallel beam separation λ, given the value of β^*. This setup corresponds to Fig. 3.5a.

Another possible crossing configuration foresees a rotation of the crossing plane to be performed at every fill during the Ramp&Squeeze sequence, in order to have a vertical external crossing angle ϕ_{V} and an horizontal parallel beam separation λ. Since the spectrometer field remains constant, the internal angle contribution ϕ_{spec} is to be added to the horizontal separation, as shown in Fig. 3.5b.

A first contribution to the calculation of the minimum aperture is obtained from the geometric construction of the B1 and B2 relative displacement from the central plane at the crossing region, in the two depicted cases (green dot in Fig. 3.5). In a drift (i.e., a region without magnetic fields), the beams just continue straight with the same angle as at the IP. This means that at an s-position, the transverse offset of a beam (corresponding to half of the total beam-beam separation) is given by:

$$\begin{aligned} R^{\mathrm{H}} &= \sqrt{\mathrm{s}^2 \tan^2\left(\frac{\phi_{\mathrm{H}} + \phi_{\mathrm{spec}}}{2}\right) + \left(\frac{\lambda}{2}\right)^2} \\ R^{\mathrm{V}} &= \sqrt{\left[\mathrm{s}\tan\left(\frac{\phi_{\mathrm{spec}}}{2}\right) + \frac{\lambda}{2}\right]^2 + \mathrm{s}^2 \tan^2\left(\frac{\phi_{\mathrm{V}}}{2}\right)} \end{aligned} \tag{3.2}$$

in the horizontal and vertical crossing setup respectively. Since the total beam separation increases as one goes further from the crossing point, s is considered to be the position of the one edge of the SC that is further from the IP, i.e., the bottleneck.

3.2.2 Orbit Drift Offset

It must be taken into account the fact that the actual orbit is naturally expected to slowly drift with respect to the nominal position. This is due to the influence of ground motion, tides and geological effects on the circumference and on the triplet positions, magnetic imperfections not completely subtracted by the orbit correctors, plus other uncorrected effects.

The impact of the orbit drift on the aperture requirement for the SC translates into a safety offset to be added to the beam separation of Eq. 3.2, and it depends on whether the cell is designed to be aligned to the actual orbit at every fill or not. In the former case, the static and long-term orbit drifts would be canceled with careful alignment at the beginning of each fill, and the SC radius should be designed with enough margins to accept the drift expected to take place within a single fill. In the latter case the radius of the cell should be large enough to account for the total orbit drift.

Since it is not clear yet what case would be the choice for the cell alignment, the two situations have been studied separately. In the case of fill-by-fill cell alignment a single-fill orbit drift of 100 μm is considered, while in the case of a non-aligned cell, a pessimistic 2 mm offset is considered, as for the aperture calculations in any HL-LHC element at top energy [46]. In Fig. 3.5 the offset is represented by the purple circle.

3.2.3 Beam Size and Betatron Effects

As a third contribution it must be taken into account the beam size along the SC. The cell will be located in the drift region upstream the IP, where the β-function is squeezed down to β^*. Then, the maximum beam size is the one seen by the furthest SC edge, which is again the bottleneck for the minimum radius calculation. In fact, handling the transfer matrix calculation in Eq. 1.11 one derives the following s-evolution in a drift:

$$\beta(s) = \beta^* + \frac{s^2}{\beta^*}, \tag{3.3}$$

which is symmetric in either side of the waist. As a convention we will refer to s as the distance from IP8.

Some effects on the optics function must be taken into account before calculating the beam size at the s-position of the furthest edge. First of all, for any aperture calculation in the LHC, it is assumed that the β-function can be up to 20% larger than its nominal value [46]. Since this situation is limiting, the most pessimistic value is assumed for the purpose of our study. The effective β-function used for the calculation is

$$\tilde{\beta}(s) = 1.2 \times \beta(s). \tag{3.4}$$

This correction might seem overly pessimistic since the optics corrections achieved so far have improved significantly, and in particular at the collision point. Nevertheless it was chosen in order to cover other effects that could alter the effective β-function: the longitudinal shift of the β minimum and the so-called β-beating. The first phenomenon is due to the fact that the minimum value of $\beta(s)$ that should ideally occur at the IP, can be subject to a longitudinal shift from −30 cm to +30 cm. The second situation arises from the presence of lattice imperfections and beam-beam magnetic effects that modify the $\beta(s)$ that is seen by a beam circulating in the LHC, leading to a beating that can change the β^* value at the IPs up to a few percent.

The combination of these effects was studied by comparing the effective $\tilde{\beta}(s)$ of Eq. 3.4 with the most pessimistic $\beta(s)$ calculated with a 5% reduction of β^* combined with a waist displacement form IP8 of 30 cm opposite to the SC location. The comparison is shown in Fig. 3.6 for three scenarios of β^*. It is found that $\tilde{\beta}$ is well conservative for $\beta^* = 3.0$ m (Fig. 3.6a), while for $\beta^* = 1.5$ m (Fig. 3.6b) the two functions are very similar. The worst case happens for the pushed optics $\beta^* = 0.5$ m (Fig. 3.6c): $\beta(s)$ exceeds our assumption within a limited s-range by a variable factor, with the maximum being $\beta(s)/\tilde{\beta}(s) = 1.53$ at ~ 40 cm from the IP, where the aperture is anyway very large. For $s > 2$ m the functions differ by less than 15%, and for $s > 4.2$ m we get $\tilde{\beta}(s) > \beta(s)$. The waist shift contribution dominates only for the most pushed optics scenario and only close to the IP.

The effective β-function allows to calculate the size of the beam as a function of the distance s from the IP. Reminding Eq. 1.19 we find the maximum beam size $\sigma(s)$ as

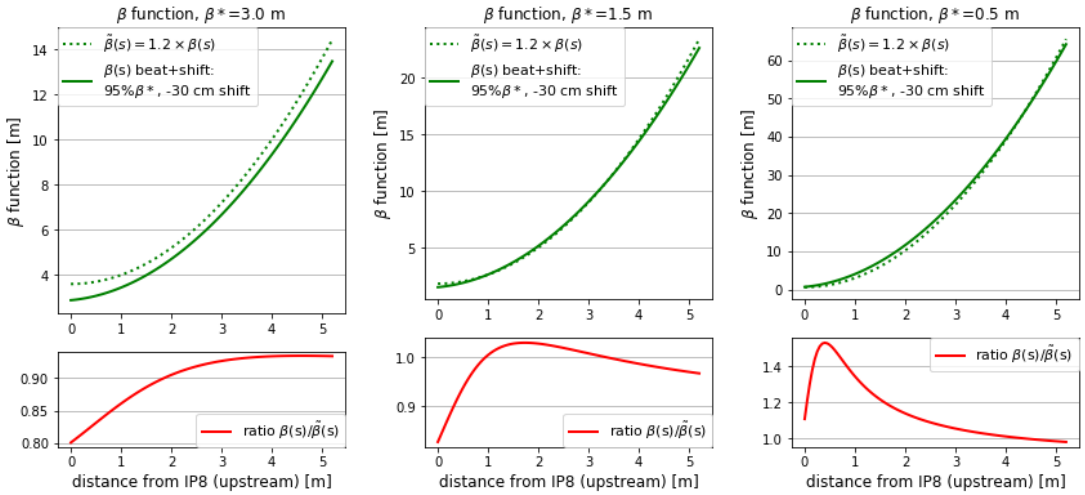

(A) (B) (C)

FIGURE 3.6: Comparison between the effective β-function of Eq. 3.4 with the pessimistic combination of beta-beating reducing β^* by a factor 5% and a waist shift of 30 cm from IP8 opposite to the SC location. Convention: s is positive in the upstream direction from IP8 (B1 reference system). In top plots the two functions are plotted, while on bottom plots it is given the ratio of the two. Three β^* cases are considered: 3.0 m (A), 1.5 m (B) and 0.5 m (C).

follows:

$$\sigma_{x,y}(s) = \sqrt{\epsilon \tilde{\beta}_{x,y}(s)} = \sqrt{1.2 \times \epsilon \left(\beta^*_{x,y} + \frac{s^2}{\beta^*_{x,y}} \right)}, \tag{3.5}$$

$$\sigma(s) = \begin{cases} \sigma_x(s) & \text{when } \sigma_x \geq \sigma_y \,, \\ \sigma_y(s) & \text{when } \sigma_x < \sigma_y \,. \end{cases}$$

It is required that the elements installed inside the LHC aperture at positions without local protection have a minimum safe aperture of 19.4σ, assuming the HL-LHC reference emittance of 2.5 μm, as explained in Ref. [47]. We thus demand that the radius of the SC should stay outside this envelope when added to the central orbit value.

In the case the SC would not involve re-aligning at every fill, one should take into account the contribution to the beam size coming from dispersion, and the parasitic dispersion from the arc [46]. Let us recall the off-momentum component to the beam size, as in Eq. 1.22. In particular, the effective dispersion function $\tilde{D}(s)$ that multiplies the momentum deviation is given by:

$$\tilde{D}(s) = k_\beta \left(|D(s)| + D_{arc} f_{arc} \sqrt{\frac{\beta(s)}{\beta_{arc}}} \right), \tag{3.6}$$

where $D(s)$ is the nominal dispersion function (calculated from $D^* = -4.79 \times 10^{-3}$ m and $D'^* = -4.95$), $k_\beta = 1.2$ is the beam size variation due to beta-beating, $D_{arc} = 2.086$ m

is the peak dispersion in the arc, $f_{\text{arc}} = 0.1$ is the fractional parasitic dispersion, and $\beta_{\text{arc}} = 170$ m the optical β-function in a focusing arc quadrupole. A 2.0×10^{-4} fractional momentum spread is assumed. The contribution from dispersion is anyway negligible with respect to the 2 mm offset that dominates the aperture restriction in this case.

Given the contributions to the aperture limitations, the minimum allowed radius for the SC is obtained from their sum, taking as limiting case the crossing configuration that maximises the constraint:

$$\begin{aligned} R_{\text{tot}}^{\text{H,V}} &= R^{\text{H,V}} + \text{offset} + 19.4\sigma \\ R_{\text{min}} &= \max\{R_{\text{tot}}^{\text{H}},\ R_{\text{tot}}^{\text{V}}\} \end{aligned} \tag{3.7}$$

3.2.4 Considered Scenarios

The minimum aperture study was performed for several operation scenarios, with different configuration assumptions. Every scenario is characterised by the optics setup (i.e., the value of β^*), the external half crossing angle $\phi_{\text{H(V)}}/2$ (either horizontal or vertical), the internal half spectrometer angle $\phi_{\text{spec}}/2$ (which can have both positive and negative polarity) and the half parallel separation $\lambda/2$.

In most cases, β^* and the crossing angles are fixed by the scenario configuration, and the maximum parallel beam separation is calculated accordingly in order to obtain the levelled luminosity $\mathcal{L}_{\text{LHCb}} = 2.0\times10^{33}$ cm^{-2} s^{-1}. The maximum λ is needed at the beginning of the fill, when the beams have their maximum intensity, and this value can be used for the calculation of the minimum aperture. The calculation of λ starts from Eq. 3.1, but we only consider the luminosity reduction due the crossing angle in the crossing plane, discarding any contribution of angles in the separation plane. This is a pessimistic assumption, since any further angle would decrease the luminosity, requiring less parallel separation for the levelling. A 20% beta-beating is considered, which can be either increasing or decreasing—but the 20% increasing case is found to require the largest parallel separation, thus it is taken as the most pessimistic case.

The external crossing angle must be negative in order to avoid parasitic collisions. The largest total crossing angle is achieved when the spectrometer has negative polarity, so that the internal and external angles have the same (negative) sign. Since the largest total angle determine the most pessimistic aperture scenario, the spectrometer will be always considered to have negative polarity in the following.

In Table 3.1 a summary is reported of all the scenarios under study with the respective configuration parameters. The following particular features were assumed for different settings:

i. *Baseline runs* where all parameters were set to the nominal ones listed in Ref. [26] for stable beam in HL-LHC;
ii. *H (V) pushed* scenario presents nominal values for horizontal (vertical) crossing angle and lower values for $\beta^* = 1.5$ m;

Parameters		Scenarios				
		Baseline	**H pushed**	**H very pushed**	**V pushed**	**V very pushed**
β_x^*	[m]	3.0	1.5	1.0	1.5	0.5
β_y^*	[m]	3.0	1.5	1.0	1.5	1.0
half ext. $\phi_H/2$	[μrad]	-250.0	-250.0	-320.0		
half ext. $\phi_V/2$	[μrad]				-200.0	-250.0
half int. $\phi_{spec}/2$ (H)	[μrad]	-135.0	-135.0	-135.0	-135.0	-135.0
half total H angle	[μrad]	-385.0	-385.0	-455.0	-135.0	-135.0
half parallel separation $\lambda/2$	[mm]	0.038	0.032	0.027	0.035	0.022
		ion runs	**Van der Meer**	**H β^*-leveling**	**V β^*-leveling**	
β_x^*	[m]	0.5	30.0	12.5	13.5	
β_y^*	[m]	0.5	30.0	12.5	13.5	
half ext. $\phi_H/2$	[μrad]	-250.0	-300.0	-250.0		
half ext. $\phi_V/2$	[μrad]				-200.0	
half int. $\phi_{spec}/2$ (H)	[μrad]	-135.0	-135.0	-135.0	-135.0	
half total H angle	[μrad]	-385.0	-435.0	-385.0	-135.0	
half parallel separation $\lambda/2$	[mm]	0.042	0.72	0.0	0.0	

TABLE 3.1: Configuration parameters assumed for the scenarios considered in the calculation of the minimum safe aperture for a SC to be installed upstream IP8 (in B1 r.s.), according to the HL-LHC operational scenarios for proton operation of Ref. [26]. The parameters for ion runs are chosen according to Ref. [48], adapting the optics to match the baseline scenario for ion runs from Ref. [48].

iii. *H (V) very pushed* scenario considers more pushed optics with $\beta^* = 1.0$ m for horizontal crossing ($\beta^* = 0.5 - 1.0$ m for the vertical case) and larger external crossing angles;

iv. *Ion runs* are considered assuming a very pushed $\beta^* = 0.5$ m (this value is chosen pessimistically as a modification of the baseline scenario for ion runs from Ref. [48] with the luminosity requirement at LHCb reported in Ref. [49]);

v. *Van Der Meer scan* is a technique for luminosity determination in which the size and shape of the interaction region is measured by recording the relative interaction rates as a function of the transverse beam separation through a progressive transverse scan of one beam through the other. They are assumed to be performed with up to $\beta^* = 30.0$ m, half external crossing angle of -300.0 μrad

and half parallel separation up to 6.6σ;

vi. *β^*-leveling* runs consist in performing the luminosity leveling by regulating β^*, while nominal external crossing angle (either horizontal or vertical) and no parallel separation are set. The value of β^* was calculated to this purpose from Eq. 3.1.

It should be noted that the very pushed scenarios, as well as the ion runs, may not be realistic given the known constraints of the optics design and aperture at the time of writing. However, these scenarios are studied anyway as limiting cases, in order to stay on the pessimistic side and take into account any possible future improvements.

3.3 Results

In Fig. 3.7 an example of the aperture calculation results is plotted. It corresponds to the configuration of horizontal crossing in the pushed optics scenario ($\beta^* = 1.5$ m), in the hypothesis of fill-by-fill alignment of the SC. The three contributions described in Sec. 3.2 are plotted separately (dashed lines), together with their sum, which correspond to the minimum radius (solid line). The different contributions are plotted as a function of the distance from IP8, which means that increasing abscissa corresponds to going further upstream from the IP in the B1 reference system. A distance range from 0 to 5 m is considered—the upper limit was chosen because it is close to the first spectrometer bump compensator and the installation of the SC at such s-positions without interference with existing elements would not be possible.

At 0.8790 m from the IP a solid black vertical line marks the VELO edge located upstream the IP in the B1 reference system, and it extends to the nominal VELO aperture of 3.5 mm. The dashed black line at 0.9435 m corresponds to the projection of the downstream edge, delimiting the zone within which the cell would be safe with an aperture larger than the VELO aperture.

The 19.4σ envelope gives the largest contribution up to 2 m from the IP, where it is overcome by the constraints imposed by the beam crossing configuration. The orbit drift offset is of course constant, and it gives a lower contribution to the sum. A very different situation is represented in Fig. 3.8 for a cell which would not be aligned at every fill. In this case the constant 2.0 mm offset dominates the sum for all the distance range analysed.

In Fig. 3.9 and 3.10 all the scenarios considered for the calculation are summarised, in the case of a cell aligned fill-by-fill or not, respectively. In these figures, only the minimum aperture given by the sum of all contributions is shown. The Van der Meer scan evidently dominates up to c.a. 4.5 m far from the IP, where it's overcome by the constraint aperture for the ion runs. These two limits impose a final safe radius of $R_{\text{min}} = 3.0 - 4.8$ mm depending on s-position, in the case of fill-by-fill alignment. If Van der Meer scans and ion runs are discarded, then the minimum safe radius has a stronger dependence on the position and varies within the interval $R_{\text{min}} = 1.5 - 4.4$ mm. Regarding the case of non re-alignment with the pessimistic 2 mm offset, the final calculation would impose a minimum radius of $R_{\text{min}} = 5.0 - 6.7$ mm, or $R_{\text{min}} = 3.5 - 6.3$ mm if Van der Meer scans and ion runs are discarded.

Let us highlight the fact that the results obtained from the presented calculation does not include any tolerance on the SC itself: they give the minimum acceptable radius that the SC can have after all the tolerances have been subtracted, such as manufacturing and alignment tolerances. The design aperture of a storage cell should thus be correspondingly larger than the given minimum acceptable radius.

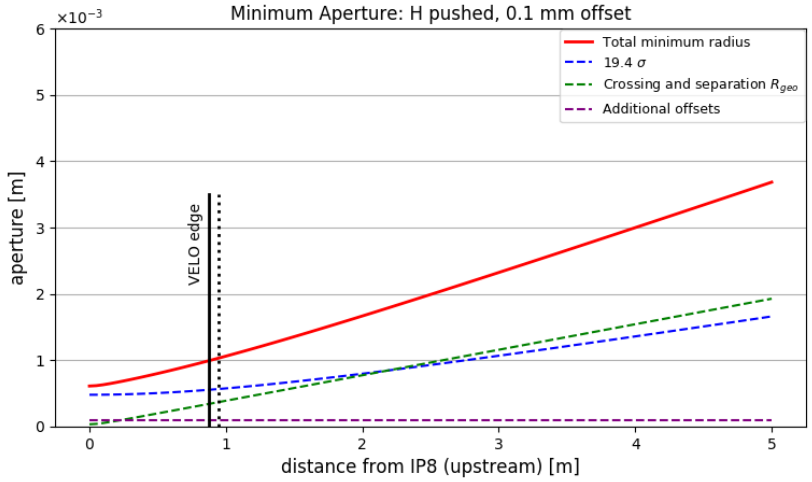

FIGURE 3.7: Minimum SC aperture for horizontal crossing, pushed scenario ($\beta^* = 1.5$ m). The dashed lines correspond to the three contributions explained in Sec. 3.2, the solid red line is their sum. The solid black vertical line highlights the VELO edge position, while the dashed one marks the mirror projection of the opposite edge with respect to the IP. A 0.1 mm offset due to orbit drifts is assumed (SC aligned at every fill).

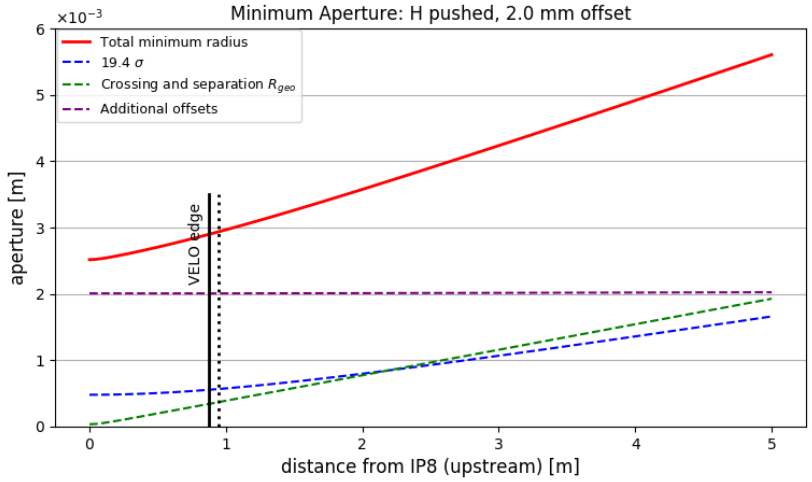

FIGURE 3.8: Minimum SC aperture for horizontal crossing, pushed scenario ($\beta^* = 1.5$ m). The dashed lines correspond to the three contributions explained in Sec. 3.2, the solid red line is their sum. The solid black vertical line highlights VELO edge position, the dashed one marks the mirror projection of the opposite edge with respect to the IP. A 2.0 mm offset due to orbit drifts is assumed (SC not aligned at every fill).

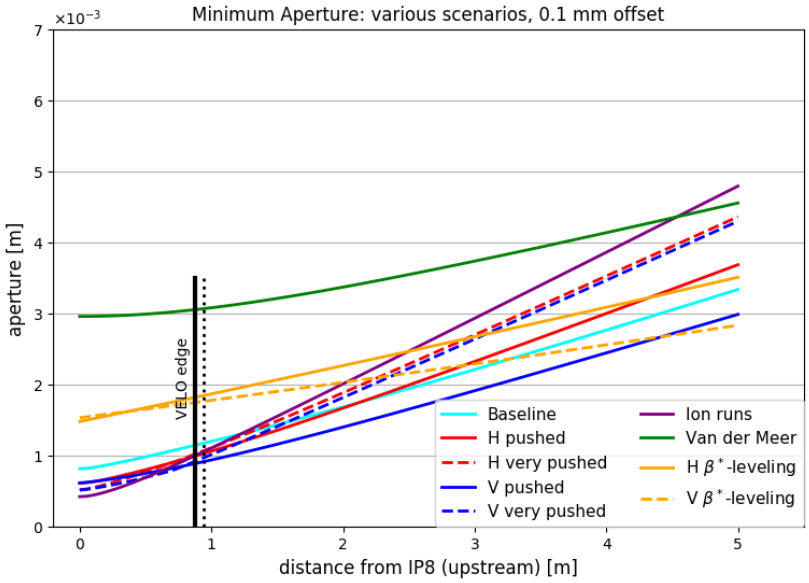

FIGURE 3.9: Minimum storage cell aperture for all scenarios as characterized in Tab. 3.1. A 0.1 mm offset due to orbit drifts is assumed (SC aligned at every fill).

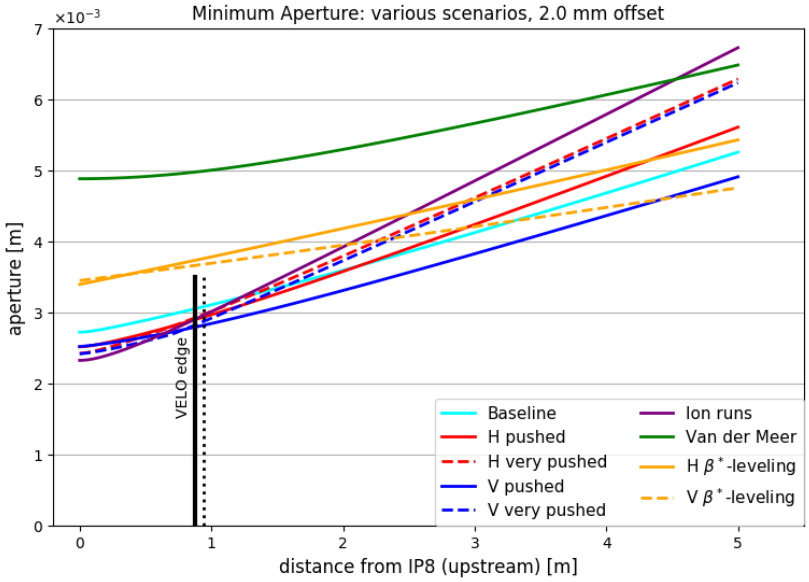

FIGURE 3.10: Minimum storage cell aperture for all scenarios as characterized in Tab. 3.1. A 2.0 mm offset due to orbit drifts is assumed (SC not aligned at every fill).

3.3.1 Aperture Calculation with MAD-X

In Ref. [31] a crosscheck of the calculation is reported: the aperture module in MAD-X (see Sec. 2.2.1) was used in order to determine the material free aperture (technically known as the beam-stay-clear) within the position range under study. This was performed by setting the nominal HL-LHC optics with $\beta^* = 3.0$ m in IP8 at 7 TeV and the parameters of the baseline scenario as listed in Table 3.1.

The SC pipe was modeled installing markers at every meter from 0 to 5 m upstream IP8. A circular aperture of 3.3 mm was assigned to the cell, corresponding to the minimum safe radius calculated for the baseline scenario in the case of fill-by-fill alignment—See Fig. 3.9. A 2.5 μm normalised emittance and a 20% β-beat were used, together with a 2×10^4 fractional momentum offset and a relative parasitic dispersion of 0.1.

In Fig. 3.11 the resulting aperture is shown. As can be seen, the beam-stay-clear is large at the IP8 and it drops down to 19.2σ at s = −5 m. This result can be compared to the analytic calculations in Fig. 3.9 in which the aperture at −5 m is found considering the safe 19.4σ. We can say that the two calculations are consistent within 0.2σ, and the small difference is likely due to the different treatment of the dispersive contribution.

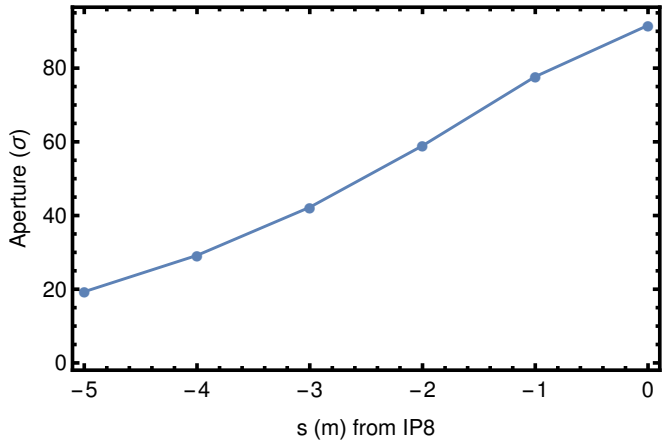

Figure 3.11: From [31]. The available aperture upstream of IP8 as calculated with MAD-X for HL-LHC v1.3, assuming a normalized emittance of 2.5 μm, $\beta^* = 3$ m, a horizontal half external crossing angle of −250 μrad, a −135 μrad horizontal spectrometer bump and a vertical parallel separation of 38 μm.

3.3.2 Outlooks and Applications: the SMOG2 Upgrade

We recall that the calculation just described was performed within the framework of the study for the PBC Fixed-Target program. However, in Sec. 1.5 we addressed the technical upgrade of SMOG during LS2 as a push for the study of the SC technology for gas target experiments at LHCb [22].

The results for the minimum aperture calculation are thus being used by the SMOG collaboration for the design and realisation of the SMOG2 storage cell which is going to be installed soon at the location of the present gas injection system in IR8. At the

time of writing, the SMOG2 cell has been successfully pre-installed and laser-aligned to the VELO RF foil, as reported by the picture in Fig. 3.12, and it is waiting to be placed at its final destination down in the LHCb cavern.

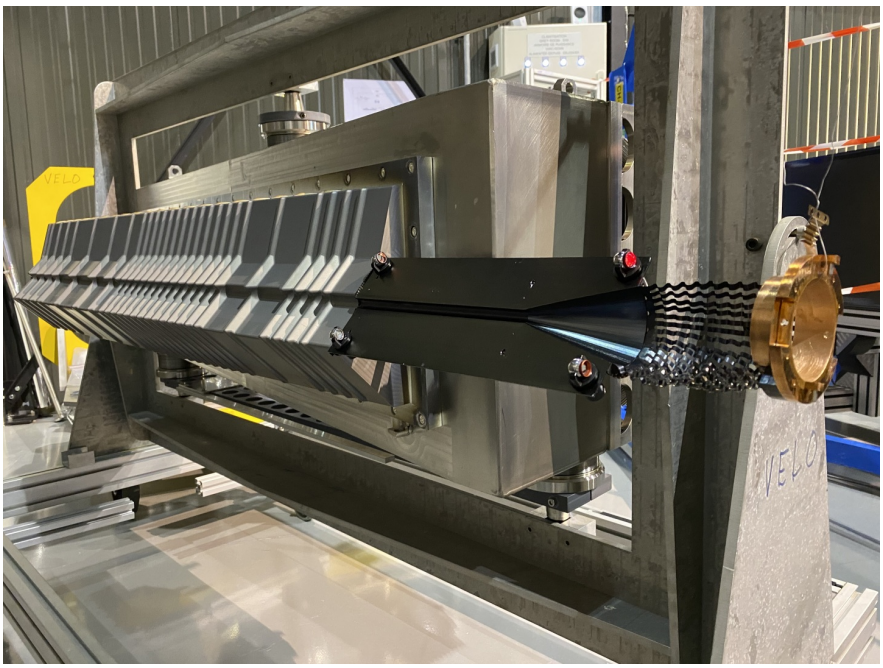

FIGURE 3.12: SMOG2, internal side view of half storage cell (black), its Wake Field Suppressor and the VELO RF foil (grey). Photograph: Di Nezza, Pasquale. Cerdits: CERN.

The implementation of SMOG2 upgrade will allow to increase by up to two orders of magnitudes the target areal density, significantly increasing the fixed-target collision luminosity. Moreover, the SC will delimit a well defined interaction region, displaced with respect to the IP, possibly allowing to run fix-target experiment in parallel with the collider mode.

SMOG2 is going to be the pilot experiment for the possible implementation of fixed-target experiments in HL-LHC.

CHAPTER 4

Conclusions

In this thesis we reported a contribution to the feasibility study for the installation of fixed-target experiments at the LHC in the framework of the Physics Beyond Collider (PBC) study program. In particular, we studied the possibility of performing collisions between the LHC beam and a fixed gaseous target in front of the LHCb detector. The proposal is to inject the target gas inside a storage cell (SC), which would allow reaching a high target areal density (up to $\theta_{\text{gas}} = 10^{14}$ atoms cm^{-2}) and to inject a variety of gas species, both polarised and unpolarised, with atomic weights ranging from H to Xe.

In Chapter 2 we presented the study of the impact on the machine of beam losses outside of the LHCb experiment, caused by the collision of the 7 TeV proton beam with the gas targets upstream of IP8 in Beam 1 reference system. Simulations were performed of the scattered proton losses on the LHC magnets and collimators. The simulation results were compared to an 8.75 W/m limit (at 7 TeV) on the continuous power loss per unit length that the superconducting magnets can withstand before quenching.

Elastic and inelastic beam-gas interactions were studied separately, as explained in Sec. 2.3.1 and 2.3.2 respectively. Both H and Xe targets were studied as limiting cases. The dependence of the losses on the longitudinal target position was studied for the inelastic case, by performing the simulations with the target located at -1.5 m and -3.0 m from the IP. The dependence is found to be very small.

For both gas species, the losses resulting from elastic interactions are found predominantly on the betatron cleaning insertion, and the local depositions recorded on the cold magnets are orders of magnitude below the quench limit. For the inelastic interactions, most of the protons interacting with the gas are lost within the target, and the surviving ones show a wider energy range and a stronger angular deviation with respect to the elastic case, which translates into more and higher losses recorded in the target region and the momentum cleaning region. The impact of a 7 TeV proton

beam on a 10^{14} atoms cm^{-2}-thick H target can be considered safe since all the losses are still below the quench limit. Conversely, the interaction with a Xe target with the same density causes cold losses exceeding the quench limit. The highest losses on cold magnets were recorded for the case of B1 hitting the target at -1.5 m from IP8—the loss was calculated to be 72 W/m at s = 23553.4 m, where a horizontal orbit corrector (MCBCH.6R8.B1) is located.

The maximum Xe density that maintains all the losses below the LHC design quench limit is calculated to be $\theta_{\max} \approx 10^{13}$ atoms cm^{-2}. This estimate is probably pessimistic and could be refined by performing dedicated energy deposition and quench limit studies for the involved magnets, accounting for the full shower and the local geometry. Moreover, such studies should be performed also on the elements closest to the LHCb experiment. The additional protection that will be installed in the Ligh-Luminosity LHC upgrade for coping with the collision debris from the IP could hopefully be effective also in intercepting the local beam-gas debris. More studies should be done in the future also to evaluate potential radiation damage at the most impacted elements, as well as effects on emittance blowup and luminosity lifetime.

In Chapter 3 an analytic calculation of the minimum safe aperture for the SC has been presented. The minimum radius was calculated as a function of the distance of the furthest cell edge from the IP. Details were given for the contributions to the total radius, arising from the geometrical configuration of the beam crossing, the possible orbit drift and the safe beam envelope that must be considered when designing elements to be installed inside the beam pipe.

A variety of operational scenarios were considered, characterised by different crossing setups, parameters and optics. A minimum SC radius was found between 3.0 mm and 4.8 mm assuming that the cell is realigned to the beam centre at every fill, so that the orbit will not drift by more than 100 μm. The dominating limitation is given by the conditions during Van der Meer scans and the vertical crossing configuration with very pushed β^* values. The result gives the minimum acceptable radius that the SC can have after all the tolerances have been subtracted, meaning that the design radius must be correspondingly larger (adding tolerances for manufacturing, misalignments, etc).

It must be remarked that the results presented in this thesis have a direct impact on the progress of the PBC Fixed-Target studies. The limitations found will be used for the design of the SC and for determining the experiment configuration in terms of target density.

The results of this work can also be directly applied to the upgrade of the present LHCb gas injection system, SMOG, to a new system called SMOG2. The upgrade involves the installation of a SC for enhancing the thickness of the injected gas. The SMOG2 installation is ongoing at the time of writing, i.e., during the Long Shutdown 2 of the LHC, and it will be operational in Run 3. The results for the minimum aperture calculation have been considered for the SMOG2 cell design.

APPENDIX A

HL-LHC Parameters

Table A.1: Parameters in collision adopted from the LHC design report [50] and parameters foreseen for the HL-LHC upgrade version 1.3 [5].

Parameter	**Nominal LHC (design report)**	**HL-LHC 25ns (standard)**
Beam energy in collision [TeV]	7	7
N_b	1.15E+11	2.2E+11
n_b	2808	2760
Number of collisions in IP1 and IP5	2808	2748
N_{tot}	3.229E+14	6.1E+14
Beam current [A]	0.58	1.1
Half Crossing angle [rad]	142.5	250
Norm. long range beam-beam separation at minimum β^*	9.4	10.5
Minimum β^* [m]	0.55	0.15
ϵ_n [μm]	3.75	2.50
ϵ_L [eVs]	2.5	3.03
R.M.S. energy spread (q-Gaussian distribution)	-	0.00011
R.M.S. energy spread (FWHM equiv. Gaussian)	1.13E-04	1.29E-04
R.M.S. bunch length [m] (q-Gaussian distribution)	-	7.61E-02

R.M.S.bunch length [m] (FWHM equiv. Gaussian)	7.55E-02	0.09
Peak Luminosity without crab-cavities [$cm^{-2}s^{-1}$] (Virtual peak for HL-LHC)	1E+34	8.11E+34
Virtual Peak Luminosity with crab-cavities: L_{peak}*R1/R0 [$cm^{-2}s^{-1}$]	-	1.7E+35
Events / crossing without levelling and without crab-cavity	27	212
Levelled Luminosity [$cm^{-2}s^{-1}$]	-	5.0E+34
Events / crossing (with levelling and crab-cavities for HL-LHC)	27	131
Peak line density of pile up event [event/mm] (max over stable beams)	0.21	1.28
Leveling time [h] (assuming no emittance growth)	-	7.3
Number of collisions in IP2/IP8	2808	2494/2572
N_b at LHC injection	1.2E+11	2.3E+11
n_b / injection	288	288
N_{tot} / injection	3.46E+13	6.62E+13
ϵ_n at SPS extraction [μm]	3.4	2.1

Bibliography

[1] *CERN official web site*. http://www.cern.ch.

[2] ATLAS collaboration. "Observation of a new particle in the search for the Standard Model Higgs boson with the ATLAS detector at the LHC". In: *Physics Letters B* 716.1 (2012), pp. 1 –29. ISSN: 0370-2693. DOI: http://dx.doi.org/10.1016/j.physletb.2012.08.020.

[3] CMS collaboration. "Observation of a new boson at a mass of 125 GeV with the CMS experiment at the LHC". In: *Physics Letters B* 716.1 (2012), pp. 30 –61. ISSN: 0370-2693. DOI: http://dx.doi.org/10.1016/j.physletb.2012.08.021.

[4] R. Bruce et al. "Reaching record-low β^* at the CERN Large Hadron Collider using a novel scheme of collimator settings and optics". In: *Nucl. Instrum. Methods Phys. Res. A* 848 (2017), pp. 19 –30. ISSN: 0168-9002. DOI: http://dx.doi.org/10.1016/j.nima.2016.12.039.

[5] G. Apollinari et al. *High-Luminosity Large Hadron Collider (HL-LHC): Technical Design Report V. 0.1*. Geneva: CERN, 2017.

[6] G. Apollinari et al. "High-Luminosity Large Hadron Collider (HL-LHC): Preliminary Design Report". In: *CERN-2015-005* (2015). URL: http://cds.cern.ch/record/2116337.

[7] *PBC web site*. https://cern.ch/pbc.

[8] J. Jaeckel, M. Lamont, and C. Vallee. *Summary Report of Physics Beyond Colliers at CERN*. Tech. rep. arXiv:1902.00260. Geneva: CERN, 2018. URL: https://cds.cern.ch/record/2651120.

[9] S. Redaelli, M. Ferro-Luzzi, and C. Hadjidakis. "Studies for Future Fixed-Target Experiments at the LHC in the Framework of the CERN Physics Beyond Colliders Study". In: *Proceedings, 9th International Particle Accelerator Conference (IPAC 2018): Vancouver, BC Canada, April 29-May 4, 2018*. 2018, TUPAF045. DOI: 10.18429/JACoW-IPAC2018-TUPAF045.

[10] D. Mirarchi. *Crystal Collimation for LHC*. 2015. URL: http://cds.cern.ch/record/2036210.

[11] A. S. Fomin et al. "Feasibility of measuring the magnetic dipole moments of the charm baryons at the LHC using bent crystals". In: *Journal of High Energy Physics* 2017.8 (2017), p. 120. ISSN: 1029-8479. DOI: 10.1007/JHEP08(2017)120.

[12] F. J. Botella et al. "On the search for the electric dipole moment of strange and charm baryons at LHC". In: *The European Physical Journal C* 77.3 (2017), p. 181.

[13] C. Hadjidakis et al. "A Fixed-Target Programme at the LHC: Physics Case and Projected Performances for Heavy-Ion, Hadron, Spin and Astroparticle Studies". In: (2018). arXiv: 1807.00603 [hep-ex].

[14] C. Barschel et al. "Report from the LHC Fixed Target working group of the CERN Physics Beyond Colliders forum". In: CERN-PBC-REPORT-2019-001 (2019). URL: https://cds.cern.ch/record/2653780.

[15] R. Aaij et al. "Measurement of antiproton production in pHe collisions at $\sqrt{s_{NN}} = 110$ GeV". In: *Phys. Rev. Lett.* 121.22 (2018), p. 222001. DOI: 10.1103/PhysRevLett.121.222001. arXiv: 1808.06127 [hep-ex].

[16] The LHCb Collaboration. "Measurement of J/ψ and D^0 production in pAr collisions at $\sqrt{s_{NN}} = 110$ GeV". In: CERN-LHCb-CONF-2017-001 (2017). URL: https://cds.cern.ch/record/2255650.

[17] R. Aaij et al. "First Measurement of Charm Production in its Fixed-Target Configuration at the LHC". In: *Phys. Rev. Lett.* 122.13 (2019), p. 132002. DOI: 10.1103/PhysRevLett.123.239901, 10.1103/PhysRevLett.122.132002. arXiv: 1810.07907 [hep-ex].

[18] The LHCb Collaboration. "The LHCb Detector at the LHC". In: *Journal of Instrumentation* 3.08 (2008), S08005.

[19] E. Steffens and W. Haeberli. "Polarized gas targets". In: *Reports on Progress in Physics* 66.11 (2003), p. 1887. URL: http://stacks.iop.org/0034-4885/66/i=11/a=R02.

[20] A. Airapetian et al. "The HERMES polarized hydrogen and deuterium gas target in the HERA electron storage ring". In: *Nuclear Instruments and Methods in Physics Research Section A: Accelerators, Spectrometers, Detectors and Associated Equipment* 540.1 (2005), 68–101. ISSN: 0168-9002. DOI: 10.1016/j.nima.2004.11.020.

[21] M. Mikirtychyants et al. "The polarized H and D atomic beam source for ANKE at COSY-Jülich". In: *Nuclear Instruments and Methods in Physics Research Section A: Accelerators, Spectrometers, Detectors and Associated Equipment* 721 (2013), 83–98. ISSN: 0168-9002. DOI: 10.1016/j.nima.2013.03.043.

[22] P. Di Nezza et al. "The SMOG2 project". In: *CERN-PBC-Notes-2018-007* (2018). URL: https://cds.cern.ch/record/2651269.

[23] M. Sands. "The physics of electron storage rings". In: *SLAC report 121* (1970).

[24] M. Martini. "An introduction to transverse beam dynamics in accelerators". In: *CERN/PS 96-11* (1996).

[25] W. Herr. "Concept of luminosity". In: *CERN Accelerator School, Intermidiate accelerator physics, DESY, Zeuthen, Germany, 15-26 September, 2003. CERN 2006-002* (2006).

[26] S. Antipov et al. "Update of the HL-LHC operational scenarios for proton operation". In: *CERN-ACC-NOTE-2018-0002* (2018). URL: https://cds.cern.ch/record/2301292.

[27] R. Bruce, R. W. Assmann, and S. Redaelli. "Calculations of safe collimator settings and β^* at the CERN Large Hadron Collider". In: *Phys. Rev. ST Accel. Beams* 18 (6 2015), p. 061001. DOI: 10.1103/PhysRevSTAB.18.061001.

[28] S. Redaelli. "Beam Cleaning and Collimation Systems". In: *Proceedings, 2014 Joint International Accelerator School: Beam Loss and Accelerator Protection: Newport Beach, CA, USA, November 5-14, 2014*. 2016, pp. 403–437. DOI: 10.5170/CERN-2016-002.403. arXiv: 1608.03159 [physics.acc-ph].

[29] C. Boscolo Meneguolo et al. "Study of Beam-Gas Interactions at the LHC for the Physics Beyond Colliders Fixed-Target Study". In: *Journal of Physics: Conference Series* 1350 (2019), p. 012010. DOI: 10.1088/1742-6596/1350/1/012010.

[30] C. Boscolo Meneguolo et al. "Study of beam-gas interaction at the LHC for the Physics Beyond Collider Fixed-Target study". In: *CERN-PBC-Notes-2019-001* (2019). URL: https://cds.cern.ch/record/2657636.

[31] C. Boscolo Meneguolo et al. "Calculation of the allowed aperture for a gas storage cell in IP8". In: *CERN-PBC-Notes-2018-008* (2018). URL: https://cds.cern.ch/record/2651289.

[32] J. B. Jeanneret *et al.* "Quench levels and transient beam losses in LHC magnets". In: *LHC Project Report 44, CERN* (1996).

[33] B. Auchmann et al. "Testing beam-induced quench levels of LHC superconducting magnets". In: *Phys. Rev. ST Accel. Beams* 18 (6 2015), p. 061002. DOI: 10.1103/PhysRevSTAB.18.061002.

[34] R. Bruce et al. "Simulations and measurements of beam loss patterns at the CERN Large Hadron Collider". In: *Phys. Rev. ST Accel. Beams* 17 (8 2014), p. 081004. DOI: 10.1103/PhysRevSTAB.17.081004.

[35] *SixTrack web site*. http://sixtrack.web.cern.ch/SixTrack/.

[36] F. Schmidt. "SixTrack. User's Reference Manual". In: *CERN/SL/94-56-AP* (1994).

[37] *MAD-X program*. http://cern.ch/mad/.

[38] G. Robert-Demolaize et al. "A new version of SixTrack with collimation and aperture interface". In: *Proc. of the Particle Accelerator Conf. 2005, Knoxville* (2005), p. 4084.

[39] A. Ferrari et al. "FLUKA: a multi-particle transport code". In: *CERN Report CERN-2005-10* (2005).

[40] G. Battistoni et al. "Overview of the FLUKA code". In: *Annals Nucl. Energy* 82 (2015), pp. 10–18. DOI: 10.1016/j.anucene.2014.11.007.

[41] A. Mereghetti *et al.* "Sixtrack-FLUKA active coupling for the upgrade of the SPS scrapers". In: *Proceedings of the International Particle Accelerator Conference 2013, Shanghai, China* (2013), p. 2657.

[42] E. Skordis et al. "FLUKA coupling to Sixtrack". In: *CERN-2018-011-CP, Proceedings of the ICFA Mini-Workshop on Tracking for Collimation, CERN, Geneva, Switzerland* (2018), p. 17. URL: https://cds.cern.ch/record/2646800?ln=en.

[43] I. Efthymiopoulos *et al.* "LHCb Upgrades and operation at 10^{34} cm^{-2} s^{-1} luminosity –A first study". In: *CERN-ACC-NOTE-2018-0038* (2018). URL: https://cds.cern.ch/record/2319258.

[44] The LHCb Collaboration. "Letter of Intent for the LHCb Upgrade". In: CERN-LHCC-2011-001 (2011).

[45] R. B. Appleby et al. "VELO aperture considerations for the LHCb Upgrade". In: (2012). URL: https://cds.cern.ch/record/1499441.

[46] R. Bruce et al. "Parameters for HL-LHC aperture calculations". In: *CERN Report CERN-ACC-2014-0044* (2014). URL: http://cds.cern.ch/record/1697805?ln=en.

[47] R. Bruce et al. "Updated parameters for HL-LHC aperture calculations for proton beams". In: *CERN-ACC-2017-0051* (2017). URL: https://cds.cern.ch/record/2274330?ln=en.

[48] J.M. Jowett. "HL-LHC heavy-ion beam parameters at LHC injection". In: *CERN EDMS 1525065* (2015). URL: https://edms5.cern.ch/document/1525065/1.0.

[49] Z. Citron et al. "Future physics opportunities for high-density QCD at the LHC with heavy-ion and proton beams". In: *HL/HE-LHC Workshop: Workshop on the Physics of HL-LHC, and Perspectives at HE-LHC Geneva, Switzerland, June 18-20, 2018, CERN-LPCC-2018-07* (2018). arXiv: 1812.06772 [hep-ph]. URL: https://cds.cern.ch/record/2650176?ln=en.

[50] O. S. Brüning et al. "LHC design report v.1 : The LHC main ring". In: *CERN-2004-003-V1* (2004).